THERMAL CHARACTERIZATION AND CRYSTAL GROWTH OF THE GERMANIUM TELLURIDE-TIN TELLURIDE SYSTEM

By

Gill Levental

A THESIS

Submitted to
Michigan State University
in partial fulfillment of the requirements
for the degree of

Materials Science and Engineering – Master of Science

2021

ABSTRACT

THERMAL CHARACTERIZATION AND CRYSTAL GROWTH OF THE GERMANIUM TELLURIDE-TIN TELLURIDE SYSTEM

By

Gill Levental

Thermoelectric materials, which can create an electrical current from a temperature gradient within the material, are an important means of generating electrical power in very remote and harsh environments. However, their deployment in terrestrial environments has been limited, due to two primary factors: the high cost of thermoelectric materials and their low energy conversion efficiency- too low for economic use in almost all applications.

One method by which thermoelectric material energy conversion efficiency may be increased is by reducing material lattice thermal conductivity, or a material's ability to conduct heat through the vibrations of its crystalline atomic lattice, which are called phonons. In support of that objective, this work presents a characterization of fundamental material properties that influence the lattice thermal conductivity of the germanium telluride-tin telluride ($Ge_{1-x}Sn_xTe$) system, a promising thermoelectric material. The properties characterized include composition-dependent coefficients of thermal expansion, speeds of sound within the material, and elastic moduli. These were characterized using high-temperature X-ray diffraction, resonant ultrasound spectroscopy, and high-pressure X-ray diffraction, respectively. This work also presents an account of the synthesis of bulk single-crystal ingots of several compositions within the $Ge_{1-x}Sn_xTe$ system, which will be used for an in-depth investigation of $Ge_{1-x}Sn_xTe$ phonon characteristics by collaborators using inelastic neutron scattering.

ACKNOWLEDGEMENTS

It is impossible to overstate the debt owed to my advisor, Dr. Alexandra Zevalkink. My journey to a completed degree has been a long road, replete with obstacles, and Dr. Zevalkink has supported me during every inch of it- including during my undergraduate experience! I am also thankful for the participation of the other two members of my committee, Dr. Carl Boehlert and Dr. Philip Eisenlohr, who generously donated their time in order to allow me to complete this process.

I would additionally like to thank the other members of the Zevalkink and Morelli research groups, who held my hand through every step of this process. Without the help provided by Dr. Ashiwini Balodhi, Dr. David Smiadak, Mario Calderon, Sevan Chanakian, Dr. Wanyue Peng, Corey Cooling, Mack Marshall, Megan Rylko, and Brendan Foley, I could not have completed the work presented before you.

Thanks are also owed to Dr. Benjamin Brugman, formerly of the MSU Department of Earth and Environmental Sciences, and the staff of the Advanced Photon Source at the Argonne National Laboratory, especially Drs. Sergey Tkachev, Curtis Kenney-Benson, Dongzhou Zhang, and Dmitry Popov, for their assistance in completing the high-pressure measurements I was lucky enough to conduct at APS.

Finally, I would like to thank my father, Dr. Shlomo Levental, and my mother, Mrs. Lily Levental, for their support—mathematical and moral alike.

TABLE OF CONTENTS

LIST OF TABLES

LIST OF FIGURES

1. Introduction

1.1 Thermoelectric Basics

A thermoelectric material is a material that allows for the direct conversion of a temperature gradient to an electrical potential gradient, or vice-versa, when joined to another material in an arrangement called a thermocouple. The conversion of a temperature gradient to an electrical potential gradient in such a system is known as the Seebeck effect, after the Estonian physicist Johann Thomas Seebeck, who re-discovered it in 1821 [1]. The reverse process, the conversion of a voltage gradient to a temperature gradient, is known as the Peltier effect, for the French physicist Jean Charles Athanase Peltier, who discovered it in 1834 [1]. The Seebeck effect has been harnessed for well over a century, most prominently in the form of the bimetallic thermocouple, which allows for rapid and precise temperature measurement through the measurement and translation of the temperature-induced electric voltage in a junction between two dissimilar metals [1]. Within the last seventy years, though, extensive work has been done on other applications of thermoelectric materials, including utilization of the Seebeck effect for electrical generation, and the Peltier effect for practical temperature control [1, 2].

No matter its use, the heart of any such device is the same: a pair of thermoelectric materials, one n-type and one p-type, joined by a metallic electrical conductor on one end, as depicted in **Figure 1** [3]. The Seebeck effect dictates that, when placed within a temperature gradient (i.e. when one side of the device is hot and the other is cold), energized hot-side charge carriers in both materials (electrons in the n-type material, holes in the p-type material) diffuse towards their cold sides, creating an electrical potential difference that is directly proportional to the difference between the hot- and cold-side temperatures. [1] When connected to a resistive load in a circuit, this potential difference creates an electrical current, as dictated by Ohm's Law

$$V=IR$$

in which V is the electric potential difference, I is the electric current, and R is the resistive load on the circuit. Connecting the device to an electrical current source instead of a resistive load will reverse this process, inducing a temperature gradient in the device. [3]

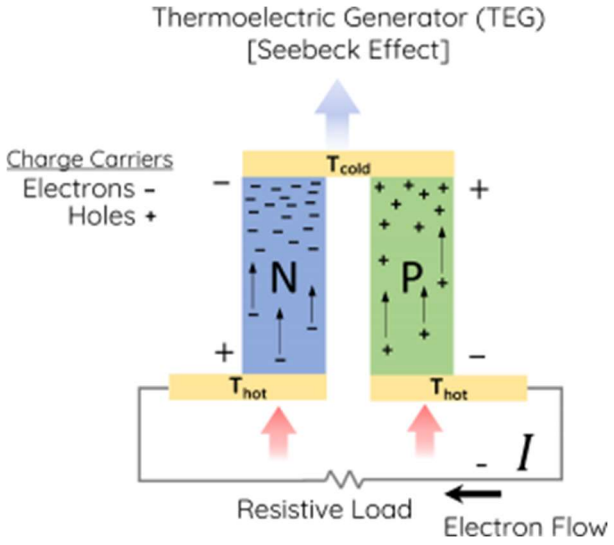

Figure 1. Diagram of thermoelectrical generator, showing distribution of charge carriers, electrical load, and temperature gradient. Image taken from ref. [4].

Seebeck and Peltier devices offer several interesting advantages when compared to their conventional mechanical counterparts. Every thermoelectric device is completely solid-state, without any moving parts or internal working fluids. Accordingly, all properly constructed thermoelectric devices can be reliable over very long periods of time, even under the harshest possible working conditions and with low or no maintenance [5]. One example of a device that leverages this extreme reliability is the Radioisotope Thermoelectrical Generator, or RTG, which is the power supply of choice for deep-space probes. RTGs generally utilize a pellet of decaying plutonium to heat their 'hot side,' and a heat sink, exposed to a cooling medium or the vacuum of space, as their 'cold side.' Since they do not require exposure to significant levels of solar radiation for power generation like photovoltaic panels do, they are suitable for use in locations

with atmospheric conditions that may preclude the use of solar panels, or at distances from the sun so great that the intensity of received solar radiation is insufficient for power generation. Many RTGs have run continuously for decades, with perhaps the most famous examples being the RTGs on the two Voyager probes, which have operated without pause for over 43 years- providing power for both probes even as they crossed the boundary between the Solar System and interstellar space, 123 AU from the Sun [6].

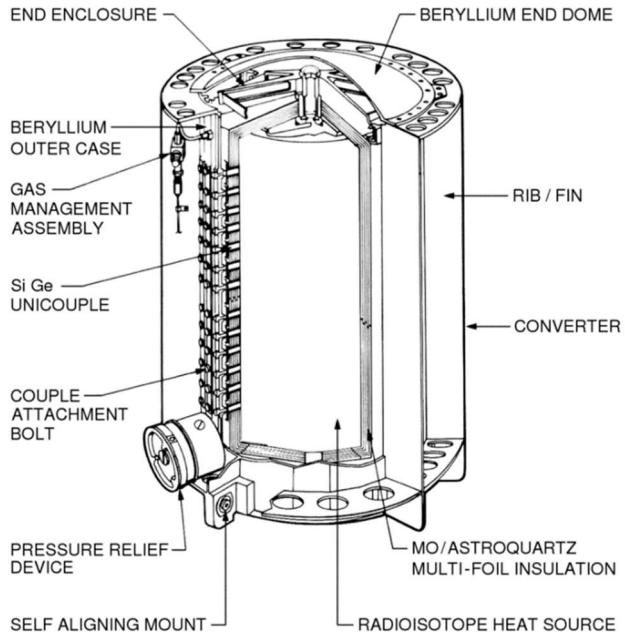

Figure 2. Cutaway diagram of a Multihundred-Watt Radioisotope Thermoelectrical Generator (MHW-RTG), as used on the Voyager probes. Electrical current is generated within the 'Si Ge unicouple'- Si Ge is the thermoelectric material used in this RTG. Image taken from ref. [7].

Though not nearly as well-known, Peltier Thermoelectric Coolers, or TECs, serve an important temperature control role in hundreds of thousands of devices. Unlike conventional cooling technologies, which require bulky pumps and coolant piping, TEC modules may be built in virtually any size or geometric configuration. TECs also have the unique ability to control heat

flow both in and out of a system via changing the polarity of the DC current used to power the device- heating one side and cooling the other when the current is flowing in one direction and flipping the heated and cooled sides when it is flowing in the other. This property allows for extraordinarily precise temperature regulation: milli-Kelvin accuracies are possible in modern devices [2].

Given their useful properties, one may be tempted to wonder why thermoelectric materials are not ubiquitous in daily life- why thermal power plants continue to use boilers, turbines and dynamos, and why the ordinary household refrigerator still uses a complex system of compressors, evaporators, and condensers instead of simple, silent, solid-state thermoelectric devices. This is the result of a combination of factors, but by far the most important are thermoelectric devices' inferior efficiency and higher cost compared to conventional power generation and temperature management technologies [3].

To understand why these limitations exist, it is important to understand the considerations that govern the cost and efficiency of a thermoelectric device. As the interconnects, heat sinks, and other elements of the device are generally constructed using relatively cheap and simple materials, the efficiency and cost of any thermoelectric device is primarily dictated by the efficiency and cost of the thermoelectric materials themselves. This stems from the expression that governs the efficiency of a thermoelectric device, which is

$$\eta = \frac{\Delta T}{T_h} \frac{\sqrt{1+zT}-1}{\sqrt{1+zT}+{T_c}/{T_h}}$$

in which the maximum efficiency η of a thermoelectric device operating in a temperature gradient ΔT formed by a hot-side temperature T_h and a cold-side temperature T_c is equal to a weighted average of the thermoelectric figure of merit zT.

zT quantifies a particular thermoelectric material's ability to efficiently transform heat into electricity, and it may be calculated using the expression

$$zT = \frac{\sigma S^2 T}{\kappa}$$

in which σ is the electrical conductivity, S is the Seebeck coefficient (a measure of the magnitude of the voltage induced by a temperature gradient across the material as created by the Seebeck effect described above), T is, by convention, the hot-side temperature of the system, and κ is the material's total thermal conductivity. The relationship between zT and η is shown graphically in **Figure 3**- as can be seen, even a relatively low zT value can reach a significant fraction of ideal efficiency.

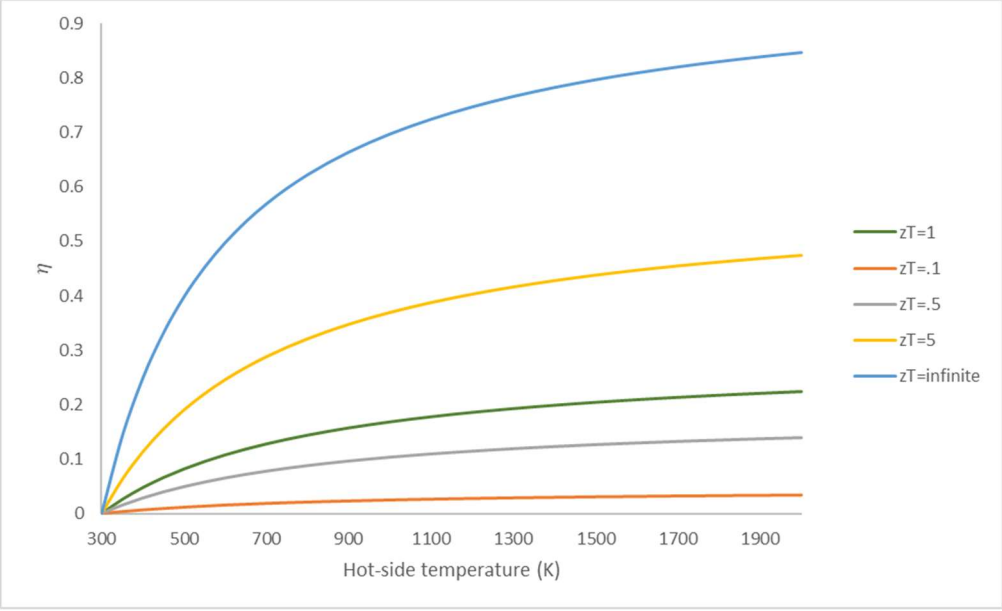

Figure 3. Plot of η vs. hot-side temperature for several different zT values for a system with a cold-side temperature of 300 K, including an infinite zT value which represents ideal efficiency.

It is important to note that the value of κ is mainly, though not exclusively, the sum of two material properties. The first one of these is the electronic thermal conductivity, or the thermal conductivity contributed by the movement of thermally-energized charge carriers (electrons and holes) through the material, which is denoted κ_{el}, and the other is the material's lattice thermal conductivity, denoted κ_l, which describes the transmission of thermal energy through the structure of the material via the vibrations of the material's crystalline structure, which are called phonons [1].

Given that a higher zT value is better, an ideal thermoelectric material would therefore have a high Seebeck coefficient and high electrical conductivity, but low thermal conductivity. As of the time of writing, the materials with the best combination of these properties, and thus the materials currently found in practical thermoelectric devices, are semiconductors [1].

Unfortunately, the existence of the κ_{el} quantity described previously indicates that thermal and electrical conductivity are directly correlated in most semiconductors. The relation between κ and σ in a semiconductor can be quantified in a more systematic way through the examination of a set of two physical expressions that summarize the thermoelectric parameters of semiconductors:

$$\sigma = ne\mu = \frac{ne^2\tau}{m^*}$$

$$\kappa = \kappa_{el} + \kappa_l = L\sigma T$$

in which m^* is the density of states effective mass, n is the charge carrier concentration, e is the charge of an electron, μ is the mobility of the charge carriers, τ is charge carrier relaxation time, κ is the total thermal conductivity, κ_{el} is the electronic thermal conductivity, κ_l is the lattice

thermal conductivity, L is the Lorenz number, σ is the electrical conductivity, and T is the system's absolute temperature. [3] Put simply, κ_{el} must be proportional to σ, and κ_{el} is a very significant contributor to κ itself. High thermal conductivity and low electrical conductivity are accordingly a rare set of properties for a semiconductor to have.

That simple fact means that even the best-performing thermoelectric materials commercialized thus far have an average zT value, in their best operating temperature range, of approximately 1 [5]. This is the rough equivalent of 10% thermal efficiency- less than half as efficient as a typical refrigerator, roughly one third as efficient as the average modern gasoline-fueled automobile engine, and less than one quarter as efficient as a modern combined-cycle thermal power plant [5] [8] [9]. This inefficiency is compounded by the high costs of the materials and processing methods involved in thermoelectric systems, especially relative to those materials and processing methods involved in the manufacture of conventional power generation and cooling technologies. [10] To be truly cost- and efficiency-competitive with conventional technologies in general applications, thermoelectric material zT figures must reach or exceed 3 [1].

Extensive research has been conducted into improving zT by improving the material power factor σS^2 and reducing the total material thermal conductivity κ of many different thermoelectric materials. [3] The power factor can be improved using a host of electronic band engineering techniques, which include the creation of degenerate states (i.e. orbitals which have the same energy level) near the material's Fermi level, and the creation of converging conduction and valence band valleys, both of which function via increasing the number of available charge carriers. These techniques and others can increase electrical conductivity significantly, while

only slightly increasing thermal conductivity, as they only increase the electronic thermal conductivity κ_{el} [11]. The total thermal conductivity can be reduced, without significantly impacting the material's power factor, by reducing only the lattice thermal conductivity κ_l, generally via reducing the velocity of phonons (and thus the rate of energy transferred by phonons) through the material's structure. This can be done in several different ways, including by creating nano-scale secondary phases and point defects within the lattice, which reduce phonon transmission velocities and thus κ_l by increasing phonon scattering [12]. Experimental use of these techniques has already resulted in significant improvements in measured zT. For instance, G. Li et. al. at Northwestern University achieved the very high zT figure of 2.2 using specially nanostructured (to reduce thermal conductivity) and doped (to increase the power factor) lead telluride [13].

1.2 Lattice Thermal Conductivity

To understand and utilize methods of increasing zT through reduction of lattice thermal conductivity, it is important to understand the mechanisms by which a lattice can conduct heat through phonon motion. The simplified lattice thermal conductivity equation

$$\kappa_l = \frac{1}{3} C_v v^2 \tau = \frac{1}{3} C_v v l$$

illustrates some of the most important relationships involved. In the equation, the lattice thermal conductivity κ_l is equal to one third of the material's constant-volume heat capacity C_v multiplied by the square of the phonon velocity v^2 and the phonon relaxation time τ – the time between phonon scattering events- or, via the relation $v = \frac{l}{\tau}$, equal to one third of the material's constant-volume heat capacity multiplied by the phonon velocity and the length of the phonon mean free path l. [14] Put simply, these equations indicate that a material's thermal conductivity

may be reduced by decreasing phonon velocity, phonon relaxation time, and/or the length of the mean free phonon path. Constant-volume heat capacity is comparatively difficult to tune and is accordingly less emphasized in literature regarding zT improvement.

All of the material properties featured within the simplified lattice thermal conductivity equation may either be directly measured or derived from experimentally measured materials properties. Heat capacity can be measured directly via calorimeter, but phonon velocity requires derivation from other properties: it is roughly equal to the material's low-frequency speed of sound, which can be calculated using the approximation

$$v \propto \sqrt{\frac{B}{\rho}}$$

in which v, the low-frequency speed of sound, is equal to the phonon velocity v, B is the material's bulk modulus (the same quantity that is commonly known as the bulk compression modulus K), and ρ is the material's density [14] [15]. These properties may be found experimentally: density via a great number of methods, including the classical Archimedes water-displacement method as described in ASTM B962, and bulk modulus via the use of analytical techniques such as resonant ultrasound spectroscopy [16].

Unfortunately, though, it is extremely difficult to discern the phonon relaxation time or mean free phonon path experimentally, with current techniques for the direct discovery of either, such as inelastic neutron scattering, or INS, requiring the use of specialized equipment, such as a high-powered, monochromatic neutron source, and special sample characteristics, such as a sample that is a large bulk single crystal [17, 18]. Unless one has the required equipment for sample

generation and measurement, one must therefore approach the problem indirectly. Key to this is an understanding of phonon scattering within lattice structures. Within a perfect crystal, the phonon relaxation time τ is only related to the level of anharmonic phonon-phonon, or Umklapp, scattering found within the crystal [19]. This can be quantified using the temperature-dependent equation

$$\tau_U \propto \frac{\mathrm{M}v^3}{V^{1/3}\gamma^2\omega^2 T}$$

in which τ_U is the phonon relaxation time caused by Umklapp scattering alone, M is the average mass (total mass of the unit cell divided by the number of atoms in the unit cell), v is the speed of sound within the material, V is the unit cell volume, γ is the Grüneisen parameter, ω is the phonon frequency, and T is the temperature of the material [19]. Umklapp scattering is the dominant scattering mechanism at high temperatures due to the inverse temperature dependence of τ, and as discussed above, thermoelectric materials are often operated at high temperatures in practical applications, rendering this equation a useful tool for the purposes of approximating τ in practical thermoelectric materials.

Discerning the values of the variables in the Umklapp phonon scattering requires both direct and indirect approaches. The material's Grüneisen parameter γ quantifies anharmonicity by describing the vibrational properties of a material's crystal structure as a function of its unit cell volume, which is, in turn, a function of temperature. The approximation pertaining to this is

$$\gamma = \frac{\alpha B}{C_v \rho}$$

in which α is the material's coefficient of volumetric thermal expansion, B is the material's bulk modulus, ρ is the material's density, and C_v is the material's constant-volume heat capacity [20].

This allows us to relate the Grüneisen parameter to the coefficient of thermal expansion, which means the coefficient of thermal expansion can in turn be related to the phonon relaxation time τ and the bulk modulus B. Thankfully, the coefficient of thermal expansion is fairly easy to measure- one can find it through the use of a simple technique like variable-temperature X-ray diffraction [20, 21].

1.3 The $Ge_{1-x}Sn_xTe$ System

PbTe, noted for its high zT and used in many high-temperature thermoelectric devices, is an example of one of the most commercially important and most thoroughly investigated types of thermoelectric material: the binary rock-salt metal chalcogenide. This type of material is characterized by two things: 1-1 stoichiometry, one metal to one chalcogen, and an Fm3m rock-salt or modified rock-salt structure in which the metal cations form a face-centered cubic structure and the chalcogen anions occupy the octahedral holes within it, which is depicted in **Figure 4**. [22] As a rule, rock-salt metal chalcogenides have relatively high electrical conductivity, due to their relatively small band gaps and high band degeneracy (caused by the particular ionicity of the metal-chalcogenide bonds), and relatively low thermal conductivity [1, 23].

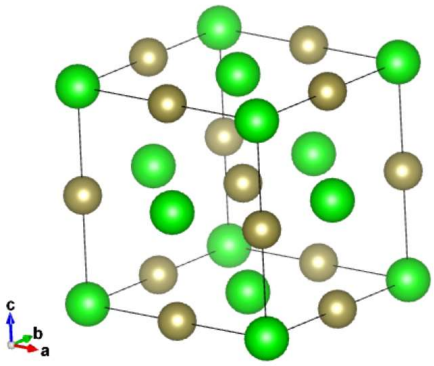

Figure 4. Fm3m 'Rock Salt' structure [24].

Out of the large number of binary rock-salt metal chalcogenides, highly doped lead chalcogenides are currently the most popular type of material for high-temperature thermoelectric generators, such as the RTGs discussed previously, both for their relatively low cost and for their superior performance within the 600-800 K temperature range found within RTGs [25]. PbTe itself is generally used instead of the other lead chalcogenides because of its superior mechanical properties- less brittle than the other lead chalcogenides, it is more capable of enduring the thermally induced mechanical strains inherent in the operation of a thermoelectric device [25, 26].

However, there is a problem with Pb-based rock-salt metal chalcogenides: the presence of lead, which in turn necessitates the use of rigorous exposure controls in both manufacturing and research settings to prevent lead ingestion and the development of a host of maladies [27]. This has stimulated research into the use of other group IV elements to replace Pb in thermoelectric materials. Two relatively well-studied replacement candidates are GeTe and SnTe, both of which have their own particular advantages and disadvantages. SnTe, which has a rock salt structure, has several attributes that make it attractive for further study. Among these are relatively low

cost and good availability, good chemical compatibility with metals, and low toxicity [10, 28] [29]. GeTe, in contrast, is significantly more costly, less abundant, and slightly more toxic than SnTe (though less so than PbTe), but it has a unique and useful attribute: a composition- and temperature-dependent phase change [30]. Like SnTe and PbTe, GeTe has a cubic rock salt structure, but unlike those materials, it only exhibits this structure at high temperatures- above 703 K. At 703 K, GeTe undergoes a phase change to a rhombohedral rock-salt structure, which it retains at room temperature and below. This structural change, which involves distortion of the Ge-Te bonds, is shown below in **Figure 5**. [30] [10, 23, 31, 32]

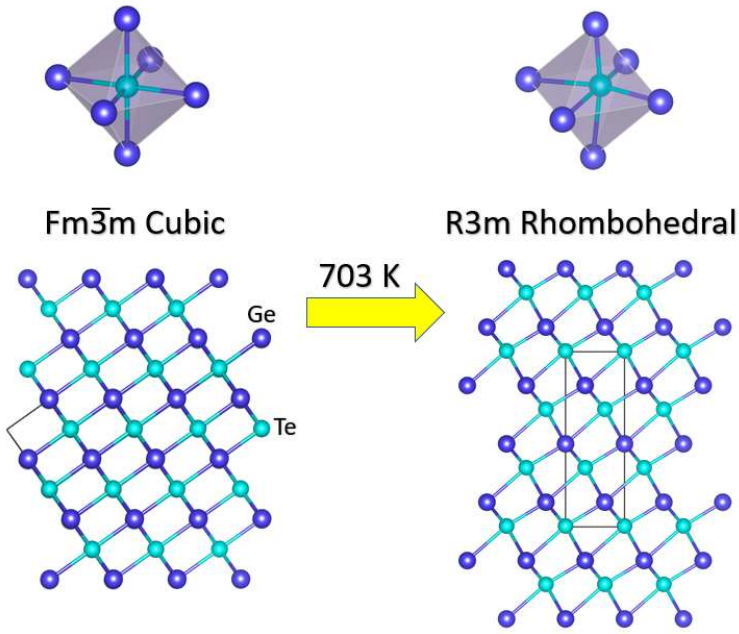

Figure 5. Schematic of GeTe in its Fm3m cubic and R3m rhombohedral structures, clearly showing Ge-Te bond distortion in the R3m structure. Ge atoms are blue and Te atoms are teal, as labeled [24].

Both SnTe and GeTe have been engineered for thermoelectric performance, both by reduction of thermal conductivity through various means and by increasing electrical conductivity through increasing charge carrier density or decreasing the width of the material's bandgap. A complete listing of modifications is beyond the scope of this paper, but some of the most successful

modifications examined so far have included alloying and doping SnTe and GeTe with other metallic chalcogenides and metals, including Sb_2Te_3, PbTe, Mn, and Ag. For example, $Sn_{.4}Pb_{.22}Ge_{.38}Te$ doped with 2 mol% Sb_2Te_3 reaches a *zT* of 1 at 800 K, while $(GeTe)_{.937}(Bi_2Se_{.2}Te_{2.8})_{.063}$ has attained a *zT* exceeding 2 at 773 K. [23, 28]

Alloys of GeTe and SnTe are particularly interesting in the context of improving thermoelectrical performance. Though not particularly heavily studied thus far, they can offer an attractive and low-cost route to the creation of more effective thermoelectric materials via the reduction of GeTe's cubic-to-rhombohedral phase change temperature. Keeping the material in the cubic phase is important for maximum thermoelectrical performance: it allows for greater charge-carrier density, and thus a larger power factor, due to structure-induced band convergence [33]. Induced by different means, this technique has proven effective in increasing *zT* over pure GeTe: Xing et. al. found that GeTe stabilized in the rock-salt phase via co-doping with Bi and Mn yielded a peak *zT* of 1.5, while Suwardi et. al's study of GeTe alloyed with Sn and co-doped with Bi and Sb to stabilize it in the rock-salt phase yielded *zT* values of up to 1.7, with ample room for improvement [33] [30, 34].

The structural properties of the SnTe-GeTe system have been the subject of study since the late 1950s, and they are fairly well understood. The system is primarily characterized by the complete solubility of SnTe and GeTe [35]. As seen, **Figure 6**, SnTe and GeTe will only form one solid phase, regardless of elemental proportions. However, as also illustrated in **Figure 6**, this phase experiences a temperature- and composition-dependent structural change. At higher temperatures, the material's unit cell takes on the form of a cubic rock-salt Fm3m structure, with

measured lattice constants of a=b=c= 6.010 Å at 733 K for Ge-rich phases and a=b=c= 5.992 Å at 663 K for Sn-rich phases [35]. At lower temperatures, it takes on a lower-symmetry R3m rhombohedral structure, which is accompanied by a shift of the Ge sublattice relative to the Te sublattice along the rock-salt unit cell's [111] direction. For rhombohedral GeTe at room temperature, the lattice constant along this direction is $\alpha = 5.986$ Å. Increasing the material's temperature, or adding Sn, causes this value to approach the cubic lattice constants provided earlier, as the composition, temperature, or both approach the phase-change point [36]. At room temperature (300 K), this is at $Ge_{.32}Sn_{.68}Te$ [36]. Adding more Ge to $Ge_{.32}Sn_{.68}Te$ increases the temperature at which the phase change occurs until it reaches the previously mentioned 733 K value for pure GeTe [36]. Adding more Sn to this base composition reduces the phase change temperature until it dips below 73 K near $Ge_{.1}Sn_{.9}Te$, with the phase change itself disappearing entirely as the system approaches pure SnTe. [35-37]

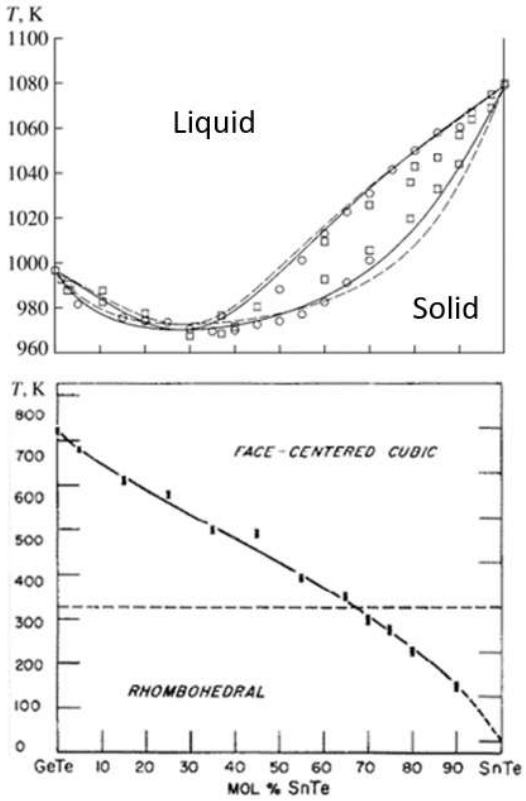

Figure 6. Phase diagram and composition-dependent structure-change diagram of the $Ge_{1-x}Sn_xTe$ system, adapted from [36] and [35].

1.4 Summary of Research

The thermoelectric properties of $Ge_{1-x}Sn_xTe$ alloys have not been studied thoroughly until relatively recently, but some very important work has been done on the topic. Among this work is Suwardi et. al's paper mentioned above, covering *zT* increase via alloying GeTe with SnTe and co-doping with Bi and Sb to reduce the phase-change temperature. [33] This paper is particularly impressive because it covers the whole of the GeTe-rich side of the system in great detail. As well as a structural study incorporating X-ray diffraction and differential scanning calorimetry data, the paper also includes lattice and electronic thermal conductivity measurements, as well as electrical resistivity, Seebeck coefficient, power factor, and charge-

carrier mobility measurements for many compositions between $Ge_{.5}Sn_{.5}Te$ and pure GeTe. A paper by Wu et. al. covered the thermoelectrical properties of the Sn-rich side of the system, using transport measurements of single crystals grown via the vertical Bridgman process- though it was not as extensive as the paper covering the Ge-rich side of the system [38]. One big hole in the knowledge base is more precise knowledge of the entire system's lattice thermal conductivity. Though the Ge-rich side of the system has been studied in this way, the Sn-rich side has not.

The objective of this paper is to add to the knowledge of the $Ge_{1-x}Sn_xTe$ system through further characterization of the system's physical constants, especially in regard to those constants that directly relate to the system's lattice thermal conductivity. This characterization will be accomplished through the use of resonant ultrasound spectroscopy, high-pressure X-ray diffraction, and temperature-dependent X-ray diffraction. Resonant ultrasound spectroscopy will be used to characterize the low-frequency speed of sound of each composition, and thus their phonon velocities. Temperature-dependent X-ray diffraction will be used to characterize coefficients of thermal expansion for the measured compositions, and high-pressure X-ray diffraction will be used to obtain material compressibility and high-pressure phase transition data. Additionally, bulk single crystals grown via the Bridgman technique will be used for in-depth investigations of the $Ge_{1-x}Sn_xTe$ system's phonon characteristics using inelastic neutron scattering techniques, which will be conducted by another group at Duke University.

2. Experimental Methods

2.1 Overview

Experimental work performed in the process of creating this thesis included the synthesis and characterization of various compositions within the $Ge_{1-x}Sn_xTe$ system, as well as GeTe and SnTe themselves.

Characterization techniques utilized within this thesis include Resonant Ultrasound Spectroscopy (RUS), using bulk samples, High-Temperature X-Ray Diffraction (HT-XRD) and High-Pressure X-Ray Diffraction (HP-XRD) using finely-ground powder samples. RUS and HT-XRD were both performed at Michigan State University, while HP-XRD was conducted at Argonne National Laboratory's Advanced Photon Source (APS).

Sample synthesis was accomplished using three methods, each of which was chosen for compatibility with specific testing procedures. For resonant ultrasound spectroscopy (RUS) and high-temperature X-ray diffraction (HT-XRD) testing, samples were synthesized via ball-milling the pure elements together in the appropriate proportions and then using spark-plasma sintering (SPS) to form the resulting powder into a cylindrical 'puck.' The pucks were used directly for RUS and crushed into a fine powder for HT-XRD. For high-pressure X-ray diffraction (HP-XRD) testing, samples were created by melting elements together into a polycrystalline ingot and then grinding the ingot into a fine powder using a mortar and pestle. The single-crystal ingots were created using the Bridgman technique for neutron scattering experiments to be conducted at a later date. The procedure for Bridgman sample synthesis will be described in detail below.

2.2 Sample Synthesis

All samples used in RUS and HT-XRD testing within this work were synthesized by Corey Cooling at the Morelli lab. To create a sample, Sn, Te, and Ge were first combined in the proper stoichiometric proportions, and then ball-milled for ten minutes to generate a fine powder for Spark Plasma Sintering (SPS), which uses joule heating of a powder compact, contained at high pressure within a graphite sintering die, to conduct extremely rapid sintering [39]. An image of an SPS machine's working area is shown below, in **Figure 7**.

All Sn used in synthesis was delivered by Alfa Aesar in 99.9999% pure, 1 mm-diameter shot form. All Te used was delivered by Sigma Aldrich in 99.999% pure, 1-2 mm-diameter shot form. All Ge used was delivered by Sigma Aldrich in the form of one 99.999% pure 50 g lump, which was manually broken up to generate quantities suitable for use in synthesis. SPS itself was conducted using a Dr. Sinter SPS-211LX spark plasma sintering press. Each set of prepared powders was heated to 735 K in the machine over the course of five minutes and then held at temperature, under a uniaxial pressure of 31 MPa, for a further five minutes- ultimately producing a 10 mm-diameter (± .01 mm) cylindrical puck with a height of 3-5 mm, depending on the quantity of powder used to create the sample. The density of every sample puck generated was measured and found to be over 97% of the theoretical density for each composition. Samples were used without further modification for RUS, and subsequently modified for use in HT-XRD by being returned to a fine powder (i.e., the powder was entirely matte in appearance) using a ceramic mortar and pestle.

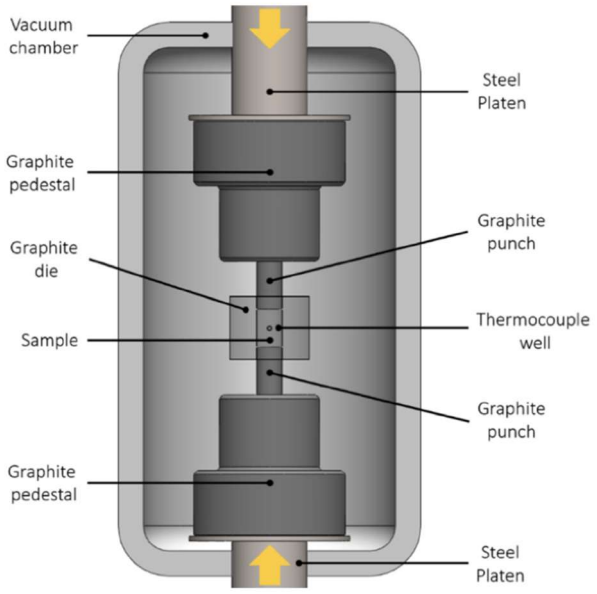

Figure 7. Spark Plasma Sintering (SPS) machine working area, showing plattens for applying pressure, conductive graphite pedestals and dies, and sample space, adapted from A. Zevalkink et al. [40].

All samples used for HP-XRD testing within this work were synthesized by the author at the Zevalkink lab. 10 g of Sn, Te, and Ge, from the sources previously mentioned, were combined into the proper stoichiometric proportions for each sample, and then ball-milled into a fine powder. The milled powder was then sealed into a quartz tube under a 10^{-4} Torr vacuum, and then melted in a Mellen tube furnace at 900 C for one hour, producing a cylindrical ingot. The ingot was removed from the quartz tube after cooling, and then ground into a fine powder (i.e., the powder was entirely matte in appearance) using a ceramic mortar and pestle.

2.3 Resonant Ultrasound Spectroscopy

The technique of resonant ultrasound spectroscopy (RUS) was selected for the measurement of the $Ge_{1-x}Sn_xTe$ system's composition-dependent elastic constants and speed of sound. RUS is one member of a group of techniques that measure the frequencies of a given sample's elastic

resonances, which correlate with the sample's size, shape, and, crucially and as their name would suggest, the sample's elastic constants [41].

Put simply, RUS uses ultrasonic pulses generated and recorded by a set of piezoelectric transducers to identify the resonant frequencies of a sample. These resonant frequencies are then used with the known analytical solution for the vibrations of a given shape (which must be precise) to discern the elastic constants of the sample [42]. At the dawn of the technique's use, it was only suitable for use with a homogenous spherical sample, but analytical solutions have since been developed for various parallelepiped shapes and cylinders [42]. Other, older ultrasonic techniques can also be used to identify the elastic constants of a solid, but they have significant complications and limitations that RUS does not share. For instance, the pulse-echo method requires the use of a large single crystal that must be physically bonded to the piezoelectric transducer that is used to resonate the sample, while RUS can utilize a smaller, polycrystalline sample that can be clamped lightly between a pair of transducers or even set atop three transducers, no physical bonding required, as illustrated in **Figure 8** [41]. RUS is therefore the fastest and most convenient method of identifying material elastic constants.

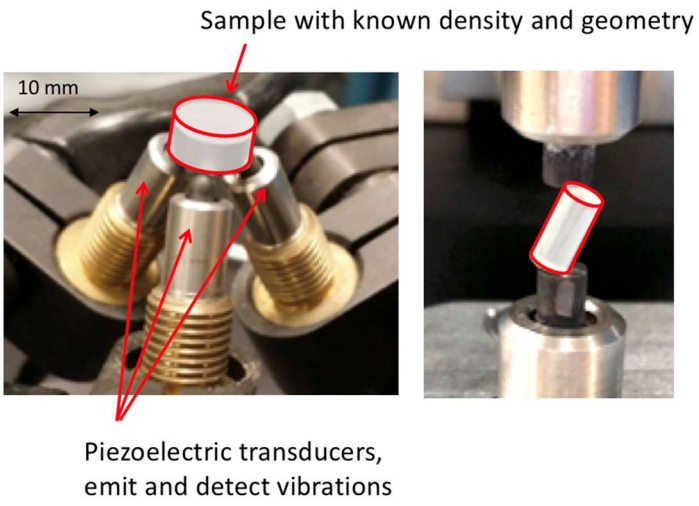

Figure 8. Arrangement of transducers on two RUS systems, adapted from W. Peng et al. [43]

All RUS measurements were conducted at the Zevalkink lab using an Alamo Creek Engineering ACE-RUS008 two-transducer room-temperature RUS system and accompanying Labview-based data acquisition and analysis software. To conduct a measurement, the sample was set between two transducers as illustrated in **Figure 8**, taking special care to ensure that the only points of contact between sample and transducer were the cylindrical sample's edges- a measure taken to ensure that the sample resonances approximated that of a notional free body as closely as possible. The acquisition software was then programmed to gather data between 50 and 400 kHz at increments of 1 kHz. Upon completion of the measurements, the analysis software was used to identify and output an ordered list of resonant frequencies. This list, together with the sample's mass and dimensions, was copied to a separate piece of software, which fit the experimental data to a set of frequencies calculated from the sample's mass and dimensions, and in doing so identified the sample's elastic constants.

2.4 High-Temperature X-ray Diffraction

The technique of high-temperature X-ray diffraction (HT-XRD) was selected for the measurement of the $Ge_{1-x}Sn_xTe$ system's composition-dependent thermal expansion characteristics. Put simply, HT-XRD involves executing powder X-ray diffraction analyses of a sample under different temperatures in order to identify temperature-induced changes in the sample's unit cell parameters, which in turn allow for the identification of the material's coefficient of thermal expansion.

All HT-XRD measurements were conducted using the CHEMS department's Rigaku Smartlab XRD system, emitting X-ray radiation in the Cu Kα range, fitted with a high-temperature vacuum sample stage as illustrated in **Figure 9**.

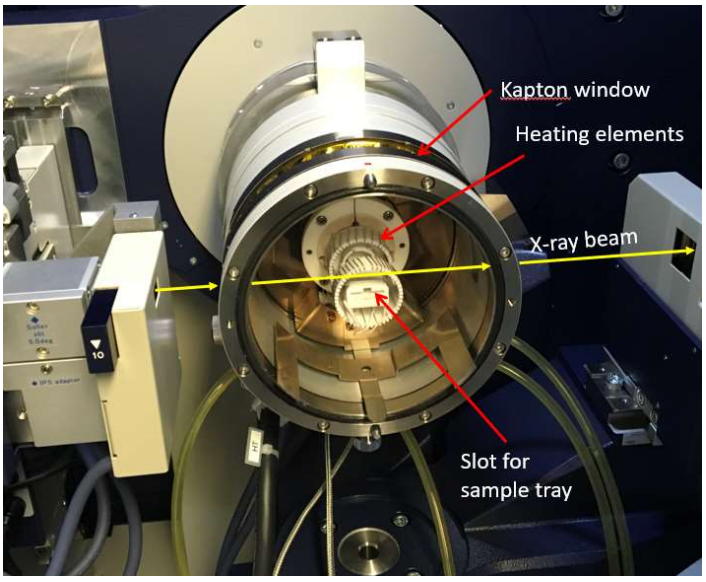

Figure 9. Rigaku Smartlab high-temperature X-ray diffraction stage, showing components and X-ray beam path, adapted from W. Peng et al [43].

All samples analyzed were subjected to HT-XRD after first being subjected to the RUS measurements described in ***2.2***, and accordingly arrived in sintered puck form. To create a

powder suitable for measurements, the pucks were manually ground using a ceramic mortar and pestle until it became difficult to discern individual particles with the naked eye, yielding a uniformly matte gray powder somewhat similar in consistency to confectioner's sugar. Each measurement was prepared by filling the high-temperature stage's Pt sample tray with the powdered sample, sealing the stage, and then drawing a 10^{-4} Torr vacuum within the stage. After the vacuum was drawn, the measurement was conducted by raising the stage temperature from room temperature to 200 C in 20 C increments and conducting a five-minute XRD scan after each temperature increase. Analysis of the raw data from each scan was done using PDXL2 software, which was connected to the ICSD database for peak matching.

2.5 High-Pressure X-ray Diffraction

The technique of high-pressure X-ray diffraction (HP-XRD) was selected for evaluation of the $Ge_{1-x}Sn_xTe$ system's composition-dependent compressibility, as well as the identification of any high-pressure phase transitions. Put simply, HP-XRD uses a special X-ray-transparent, high-pressure cell known as a diamond anvil cell (DAC) and an X-ray synchrotron light source to conduct X-ray diffraction measurement on small samples at extremely high pressures- potentially in the hundreds of gigapascals.

The DAC itself, which is shown in **Figure 10**, is at the heart of the technique. There are several different types of DAC, but all share some common features. Generally speaking, a DAC is a hollow, multi-part steel cylinder that holds a pair of gem-cut diamonds, the diamond anvils of the diamond anvil cell, against each other, culet to culet, allowing for X-ray measurements of a sample between the diamonds to be taken using an X-ray beam transmitted through the diamonds. Between the two diamonds is a gasket: a thin piece of metal, such as Re, W, or Be, that separates the diamonds- important, because direct contact between the diamonds at high pressures can shatter both diamonds- and forms a gas-tight seal around the sample space, the area in which the sample contacts both diamonds. The gas-tight seal provided by the gasket also allows for the injection of a pressure medium into the sample space, such as a gas like Ne or Ar, for experiments that require isotropic pressure on the sample. The sample space can also contain a piece of a pressure-registering medium, such as ruby, for in-situ pressure measurements using laser fluorescence- the fluorescent spectrum of the material could be recorded and fit to an equation of state curve, automatically generating pressure data. Some DACs, such as the BX90

DACs used during the experiment, contain a special membrane that can adjust the pressure on the sample in real situ by being inflated or deflated to a specified level at a specified rate.

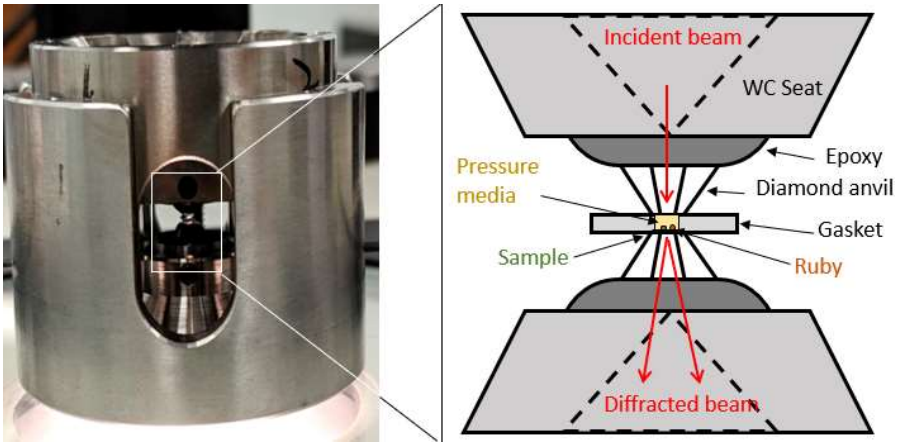

Figure 10. Cutaway labeled view of a diamond anvil cell, adapted from W. Peng et al. [43].

All HP-XRD testing was performed at the 13-BM-C GSECARS beamline at Argonne National Laboratory's Advanced Photon Source (APS). Samples were synthesized via melting and crushing as described above, producing sub-micron powders which were pressed into flakes for easier DAC loading. DAC loading was performed on-site at APS by Dr. Wanuye Peng of the University of California, Riverside and Dr. Sergey Tkachev of the University of Chicago. Two DACs were used in the experiment. Both featured diamonds with 300 µm-diameter culets, a laser-drilled Re gasket, a ruby in the sample space for pressure measurements, and neon was used in both as the hydrostatic pressure medium. Prior to scanning, the GSECARS Pilatus 1M detector's distance and orientation was calibrated with a CeO_2 standard, using the different relative X-ray transmissivity of the diamonds and sample to identify the position of the sample in the 12 µm x 18 µm FWHM GSECARS X-ray beam.

Measurements were conducted by the author and Dr. Wanyue Peng using the beamline's control

software. Starting with their respective initial pressure, each sample was raised by a set pressure increment and then subjected to a five-minute scan until a phase change was noted within the sample or sufficient data was gathered to determine sample compressibility. Pressure inside the sample space were recorded before and after each measurement using the ruby laser fluorescence system.

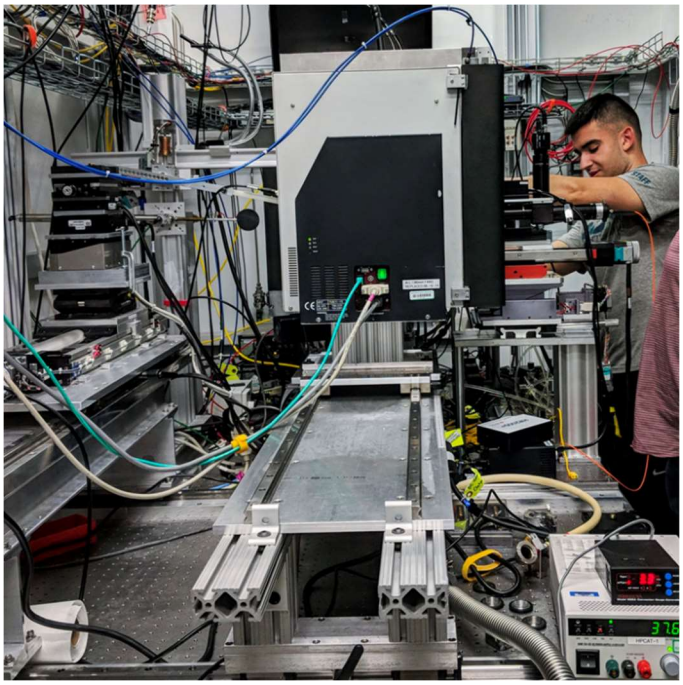

Figure 11. The author mounting a DAC in the beamline at the Advanced Photon Source. Photo credit Dr. Wanyue Peng.

2.6 Bridgman Bulk Single Crystal Synthesis for Inelastic Neutron Scattering Measurements

The Bridgman method is a simple and relatively old method of growing bulk single crystals. It was the second such method to be successfully implemented, after the Verneuil flame-fusion method, and the first to be useful for synthesizing single-crystal boules of substances other than several types of gemstone [44]. Invented by Percy Williams Bridgman during the first half of the 20th century, the Bridgman method consists of the controlled solidification of a melt into a single

crystal ingot via translating it through a temperature gradient [44]. When conducted properly, the slow translation of the melt through the temperature gradient would first induce nucleation on only one site- for example, a preexisting seed crystal- and then continue the crystallization of the melt in a way that only allows for further growth on the liquid-solid interface of the existing crystal, rather than inducing nucleation and grain growth on the crucible walls as in a conventional casting process [44].

There are many different types of Bridgman apparatus, allowing for many variations on the process described above. For instance, melt translation may be accomplished in the vertical or horizontal direction, single crystal growth may be started with a seed crystal or by use of a carefully shaped crucible (which forces grain selection via geometry), the crucible containing the melt may be evacuated, filled with gas, or unsealed, and the temperature gradient may be regulated via manipulation of one furnace, two furnaces with a baffle between them (generally referred to as the Stockbarger method), or by some other method [44, 45]. The furnace can also be translated instead of the crucible, a technique occasionally used in horizontal Bridgman machines. A Stockbarger-type Bridgman apparatus (and its temperature gradient) are shown below, in **Figure 12** [44].

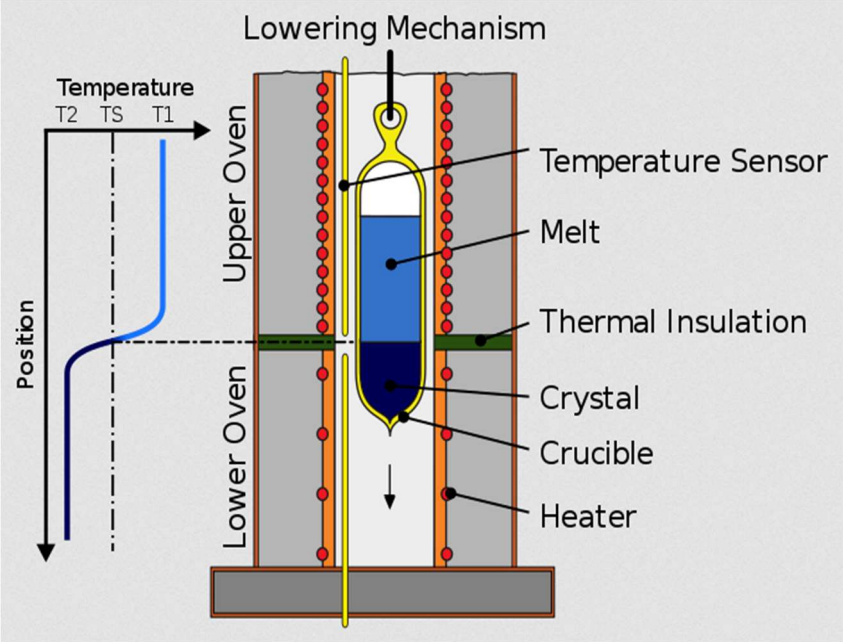

Figure 12. Depiction of Stockbarger-Type Bridgman Furnace, with temperature gradient, adapted from [46].

Some of the differences listed can have a dramatic impact on the final properties of the crystal ingot. For instance, a vertical Bridgman system can easily generate ingots with a circular cross-section, which has beneficial characteristics for microfabrication, while a horizontal Bridgman system generally yields ingots with a much lower dislocation density. The shape of the crucible in a horizontal Bridgman system provides a much larger free surface for the melt, allowing for expansion unconstrained by the crucible walls, and thus less internal stress, a primary source of dislocations within a crystal [44].

A relatively large number of studies of the $Ge_{1-x}Sn_xTe$ system have involved growth of bulk single-crystal samples of both tellurides and the alloy, both for investigations of the properties of the material itself and for more general investigations into crystal growth within a Bridgman system [15, 36, 37]. Unfortunately, while many of the papers included descriptions of experimental apparatus, lowering rates, furnace temperatures, and other pieces of the process,

they generally neglected to provide the most crucial detail: the furnace temperature gradient, generally expressed in C/cm, that allowed for successful single crystal creation. The first eight crystal growth attempts were therefore conducted using trial and error. After further literature review, subsequent growth attempts were conducted using Rehwald and Lang's paper, which specified a temperature gradient of 32 C/cm [37].

All Bridgman crystal growth attempts were conducted using the apparatus depicted in **Figure 13**, below, which was constructed in 2017 by the author and Mario Calderoncueva using four tube furnaces, each rated for 1100 C: two produced by the Snyder group at Northwestern University, one from the Mellen company, and one SCX1100 from the Crystal Systems Corporation. The central feature of the system is a computer-controlled Oriental Motors EAS-series electric linear actuator with a custom sample mounting beam. This system allows the sample to move upwards or downwards through a tube furnace at a minimum continuous rate of .001 mm/s or, when programmed to pause between movements, less than .00001 mm/s. The EAS assembly is attached to a strut-channel upright, which is in turn fastened to a quarter-inch steel baseplate with vibration-isolating mountings, which acted to minimize sample sway (and consequent contact with furnace walls) due to laboratory vibrations. The quarter-inch steel baseplate has sufficient space and load-bearing capability for up to two tube furnaces at a time, allowing for the simultaneous growth of two crystals. Firebricks and quartz wool are usually arranged below each furnace to cushion the impact of a falling crucible and insulate the steel from the heat of the furnace. The top of each furnace was covered by a quartz wool or brick plug to create a desirable temperature profile (ie, isothermal at the top, a very sharp gradient to room temperature at the bottom) within the respective furnace tubes.

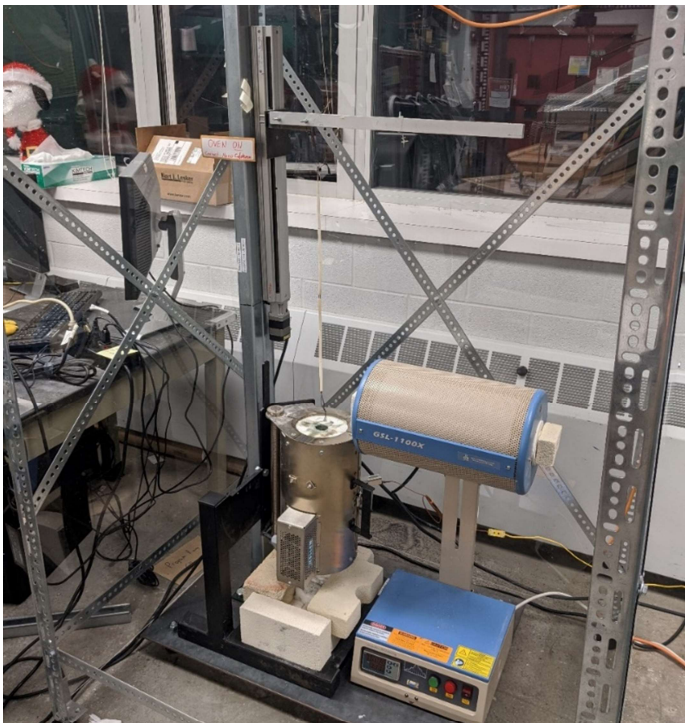

Figure 13. Zevalkink Lab Bridgman Furnace setup c. 2019. The SCX-1100 and Mellen tube furnaces are mounted atop the baseplate in the image.

Crucible diameter and sample composition aside, the steps of sample preparation were identical for each of the 25 samples generated during this research. In each instance, a sharp-pointed crucible was formed from a length of quartz tube using a methane-oxygen torch. This was generally done using 10 mm-diameter tubing but was also done several times using 12.7 mm tubing. Calculated quantities of germanium (three nines, in ~.1 g pellet form, from Alfa Aesar), tin (three nines, in ~.1 g pellet form, from Sigma Aldritch), and tellurium (four nines, in ~.1 g pellet form, from Alfa Aesar) were poured into this shaped crucible and sealed under a >.0001 Torr vacuum within the quartz tube, using a vacuum pump and the methane-oxygen torch. The torch was also used to form a quartz hook at the sealed top of the crucible for attachment to the sample motion system. Finished crucibles, such as the crucible pictured in **Figure 14**, were then suspended from the Bridgman system's motion arm using a loop of thick type-K thermocouple

wire. Occasionally the hook could not be formed using the torch. In these instances, the type-K wire was formed into a cradle around the crucible, generally with one loop around the sharp point and another higher up on the crucible's 'tube' section. It was important to discard the wire after each growth- reuse of the wire could and did result in failure of the wire and attendant loss of the sample, especially when the furnace was operated at temperatures exceeding 900 C.

Figure 14. Sealed crucible, showing sharp tip, 'dimple' from pressure checking, and sample precursor materials within.

The first stage in the actual execution of a growth was to properly characterize the temperature gradient inside the furnace at the selected growth temperature. This was accomplished by passing

a type-K thermocouple attached to a temperature recorder through the furnace using the EAS linear motion system at the minimum continuous rate, and then plotting the measured temperature against the thermocouple's position within the furnace. It was often desirable to do this using the actual planned movement program for the growth itself, to properly verify program functionality. An example of this is shown below, in **Figure 15**. If the temperature gradient was equal to or greater than the desired value, the system was ready for growth; if not, the furnace temperature was changed, and the process repeated until the desired gradient was attained.

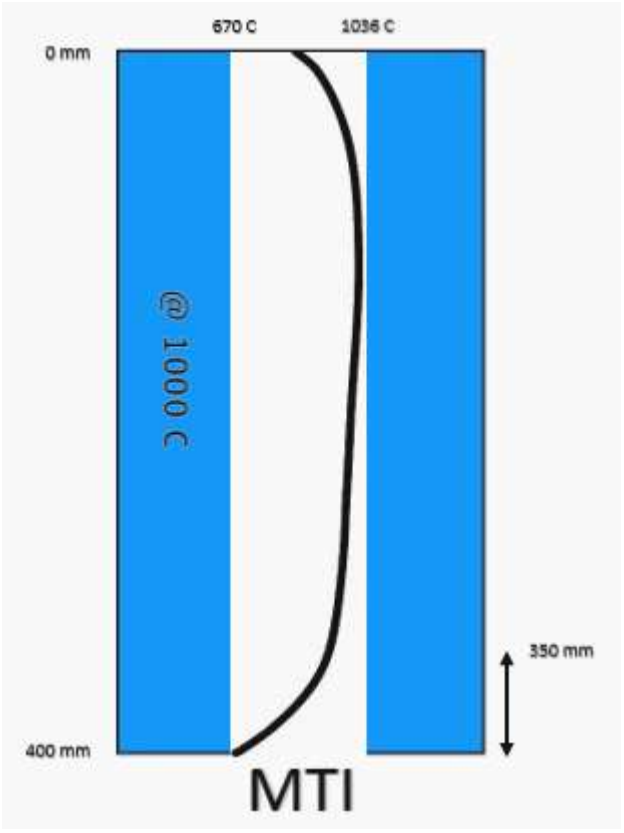

Figure 15. Schematic depiction of an MTI tube furnace and temperatures within the tube with the furnace set to 1000 C. Tube was oriented vertically and top was sealed with firebrick and quartz wool. Shape of curve indicates temperature changes between 670 C (lowest recorded temperature) and 1036 C (highest recorded temperature).

Once the temperature gradient was set and verified, the thermocouple and reader could be withdrawn and replaced on the linear motion system by a filled crucible, prepared in the method

described above. This crucible was passed through the cold furnace several times to verify that it would not strike or rub against the furnace wall during the descent. When this process was complete, the crucible was raised within the furnace to a position at which, based on the previously collected data, the whole crucible would be heated to a temperature slightly exceeding the melting temperature of the selected $Ge_{1-x}Sn_xTe$ composition. The furnace was then brought to the selected temperature, and the sample within left to melt and homogenize via convection within the melt for two to three hours. Upon completion of the homogenization period, the EAS linear motion system's control program was started, and the system left alone as the crucible completed its journey through the furnace. Upon completion of the motion program, the furnace was switched off and allowed to cool to room temperature before the crucible was removed. The solidified ingot was extracted from the crucible by shattering or breaking the crucible at a point an inch or two above the ingot's upper surface. Care was taken to ensure that the ingot itself did not lose too much mass to breakage during the extraction process, and that quartz fragments from the crucible and pieces of the broken ingot (which were useful for XRD analysis) were kept separate.

The grown crystals were analyzed for crystallinity and homogeneity using optical microscopy with a Keyence digital microscope, Scanning Electron Microscopy (SEM) and Energy Dispersion Spectroscopy (EDS) with a Carl Zeiss EVO LS 25 Scanning Electron Microscope with onboard analysis software, X-Ray Diffraction (XRD) with a Rigaku Smartlab XRD and PDXL2 software, Laue camera analysis using a system built in-house at Michigan State, and in one instance, Electron Backscatter Diffraction (EBSD), also on the EVO LS 25 SEM. EDS and XRD were useful for assessing homogeneity- EDS allowing for *in situ* estimations of crystal

composition at specified points, and XRD allowing for more precise composition characterization, though requiring the loss of some parts of the sample. Optical, SEM, EBSD, and Laue techniques were useful for assessing the single-crystal character of the samples, via fracture surface analyses in the case of optical and SEM imaging, and via more effective backscatter techniques in the case of EBSD and Laue imaging.

Ingots were prepared for all of these process by being sectioned with a diamond-bladed sample saw to expose the inner structure of each sample, followed by rough and fine polishing of the exposed surface with 600 grit, .1 um, and .05 um abrasives on a polishing wheel. The removed portions of the sample were then split in two, and the halves ground into a find powder to allow for comparison between top and bottom composition via XRD. Additionally, parts of the samples often broke off the main ingot during extraction from the crucible or sectioning. These separated parts were also ground up for XRD, and the surfaces they revealed on the main ingot were useful for revealing visual indications of crystallinity.

3. Determination of Speed of Sound in the $Ge_{1-x}Sn_xTe$ System

Resonant ultrasound spectroscopy (RUS) analyses conducted as described in Chapter **2.1** produced a clear picture of the $Ge_{1-x}Sn_xTe$ system's elastic constants, and thus changes in speed of sound throughout the system- an important component of the lattice thermal conductivity κ_l, as described in the κ_l equation. To form a complete picture of the elastic moduli, five samples were analyzed using the apparatus described above: GeTe, $Sn_{.25}Ge_{.75}Te$, $Sn_{.5}Ge_{.5}Te$, $Sn_{.75}Ge_{.25}Te$ $Sn_{.9}Ge_{.1}Te$, and SnTe. X-ray diffraction was used to verify the structure and composition of each sample; it confirmed that GeTe, $Sn_{.25}Ge_{.75}Te$, and $Sn_{.5}Ge_{.5}Te$ samples had the expected rhombohedral structure, and that $Sn_{.75}Ge_{.25}Te$, $Sn_{.9}Ge_{.1}Te$, and SnTe samples had the proper cubic structure, and it also showed that the samples were phase-pure with the exception of an Sn impurity phase in the SnTe sample.

Each measurement produced a spectrum of intensity versus frequency, two examples of which are shown below, in **Figure 16** and **Figure 17**. Software was used to automatically identify the frequencies of specific resonant frequencies, which appear as peaks in the raw spectrum, for later use. In some cases, degenerate peaks were found to "split" due to small deviations of the sample geometry from a perfectly cylindrical shape. In those cases, the average of the two frequencies was used.

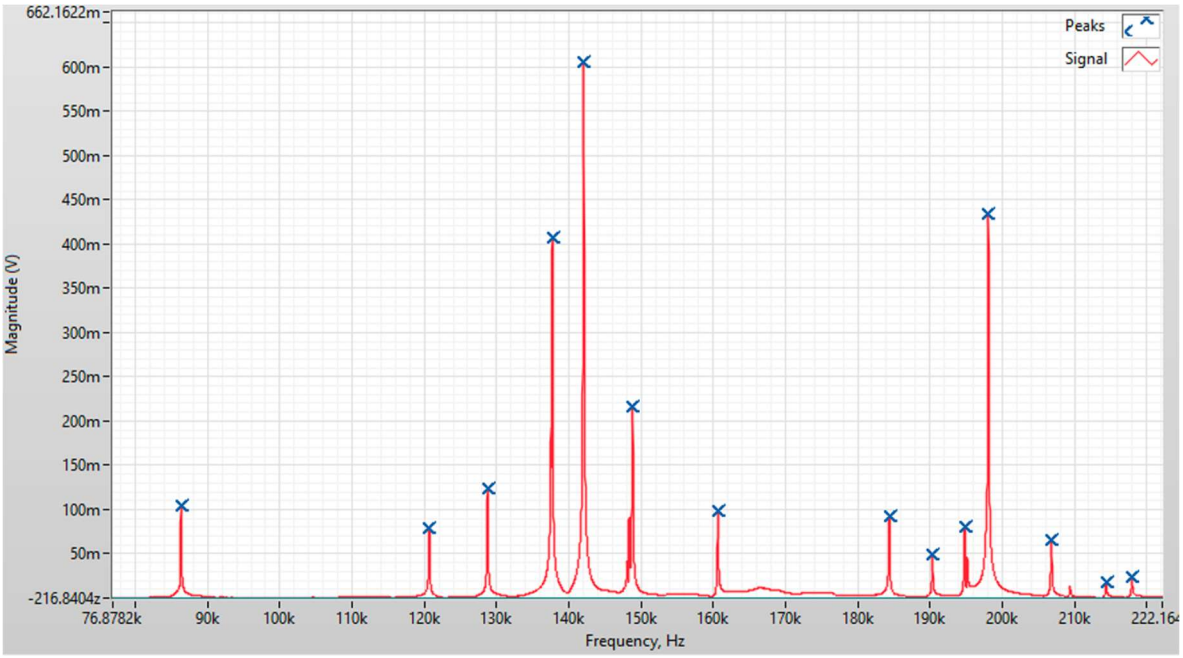

Figure 16. Raw RUS spectrum data and automatically calculated peak positions for $Sn_{.25}Ge_{.75}Te$.

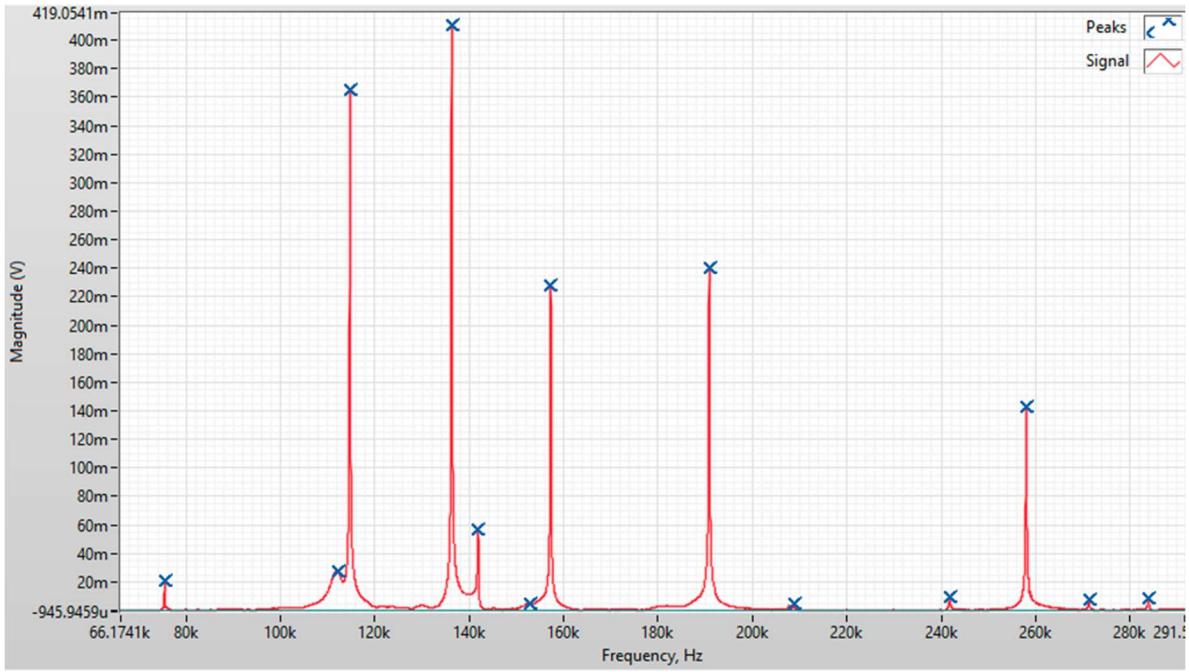

Figure 17. Raw RUS spectrum data and automatically calculated peak positions for GeTe.

The observed frequencies were used, together with measured sample masses and dimensions, to compute each sample's elastic constants and speed of sound. This was done by means of iteration: the software, which was called 'Cyl9,' first calculated expected resonance values based on manually submitted sample data and predicted elastic constant values, and then changed the elastic constant values in a systematic way in an attempt to fit the calculated resonance values to the experimental data. A degree of error (i.e. a difference between fitted and experimental resonance values) was present for every sample- it was considered acceptable if it did not exceed 1%. By this criteria, measurements of two samples produced acceptable data: GeTe and $Sn_{.25}Ge_{.75}Te$.

The results of these calculations are summarized below in **Table 1**, which shows elastic moduli, transverse speed of sound, longitudinal speed of sound, Young's Modulus, Bulk Modulus, and Poisson's ratio vs. composition.

Table 1. Elastic constants of GeTe and $Sn_{.25}Ge_{.75}Te$

Composition	C11 (GPa)	C44 (GPa)	Young's Modulus (GPa)	Bulk Modulus (GPa)	Transverse Speed of Sound (km/s)	Longitudinal Speed of Sound (km/s)	Poisson's Ratio
GeTe	63.4	20	50.9	36.7	1.8	3.3	0.27
$Sn_{.25}Ge_{.75}Te$	56	16.5	42.9	34	1.6	3.0	0.29

Elastic modulus and speed of sound values were plotted vs. composition in **Figure 18** below, to identify trends. These were also plotted versus composition with literature values for SnTe and

GeTe for comparison. Literature elastic modulus values were obtained from Schmidt et. al.'s work on SnTe elastic moduli and Peng et. al.'s work on GeTe elastic moduli [47, 48].

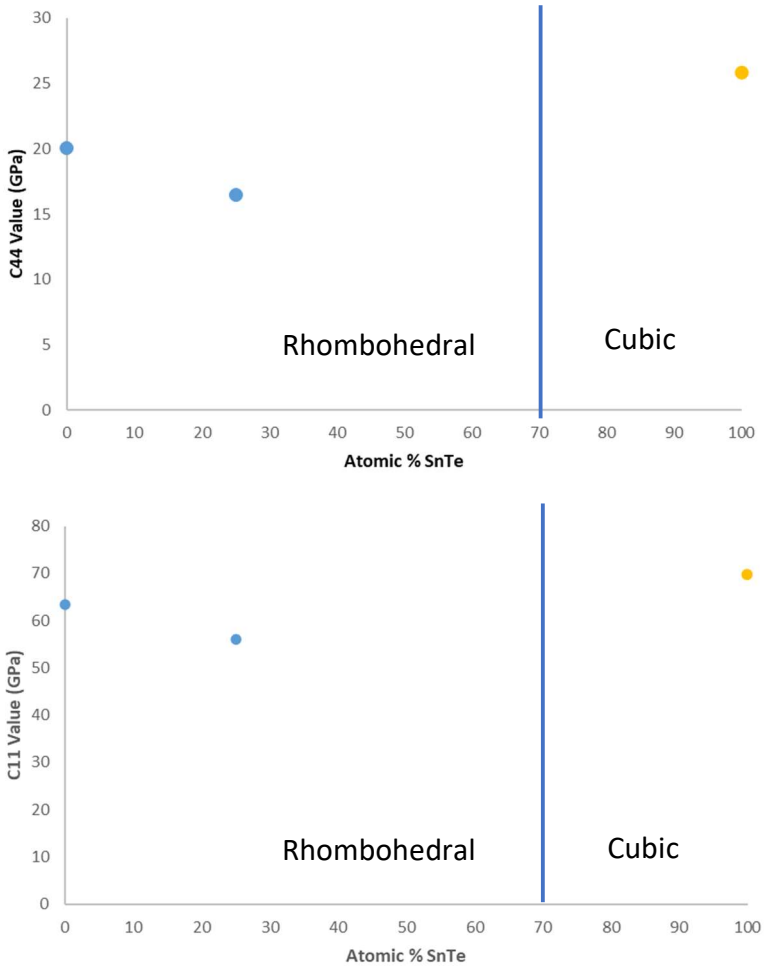

Figure 18. Plots of C44 and C11 elastic moduli vs. composition. Orange denotes data from literature, the blue vertical line denotes the phase-change composition at room temperature.

A common trend is immediately apparent in each of the plots: a decrease in both elastic moduli and speed of sound from pure GeTe to $Sn_{.25}Ge_{.75}Te$, and then an increase between $Sn_{.25}Ge_{.75}Te$ and SnTe, which continues- at least according to the elastic moduli data- between $Sn_{.9}Ge_{.1}Te$ and SnTe. The reasons for this are structural. GeTe and $Sn_{.25}Ge_{.75}Te$ have rhombohedral structures, as described previously, in which the Ge-Te bonds are longer than the Sn-Te bonds are in SnTe's

cubic structure. These long bonds have a greater ability to stretch than the shorter bonds, making them 'softer,' which in turn should give rhombohedral structures lower C11 and C44 values than cubic structures- a notion which is borne out in the experimental and literature data [47, 48]. Within the rhombohedral structure, the reduction in C11 and C44 values and the according reduction in speed of sound between GeTe and $Sn_{.25}Ge_{.75}Te$ is also a structural effect: the addition of Sn to the alloy changes the orientation of the structural bonds, making them 'softer' than GeTe alone.

4. Determination of Coefficients of Thermal Expansion in the $Ge_{1-x}Sn_xTe$ System

High-temperature X-ray diffraction (HT-XRD) analyses conducted as described in **2.2** produced a clear picture of the temperature-induced lattice parameter and phase changes, and thus the changes of the coefficient of thermal expansion as a function of Sn content in the $Ge_{1-x}Sn_xTe$ system. Four compositions were selected for analysis: SnTe, $Sn_{.9}Ge_{.1}Te$, $Sn_{.5}Ge_{.5}Te$, and $Sn_{.25}Ge_{.75}Te$. These compositions are marked with the temperature range selected for their measurement in the phase diagram in **Figure 19.** In addition, we compare our results with GeTe data, which was obtained from the literature [49], and were selected for optimal coverage of the Ge_{1-x} Sn_xTe system, given the limited measurement time and equipment temperature range available.

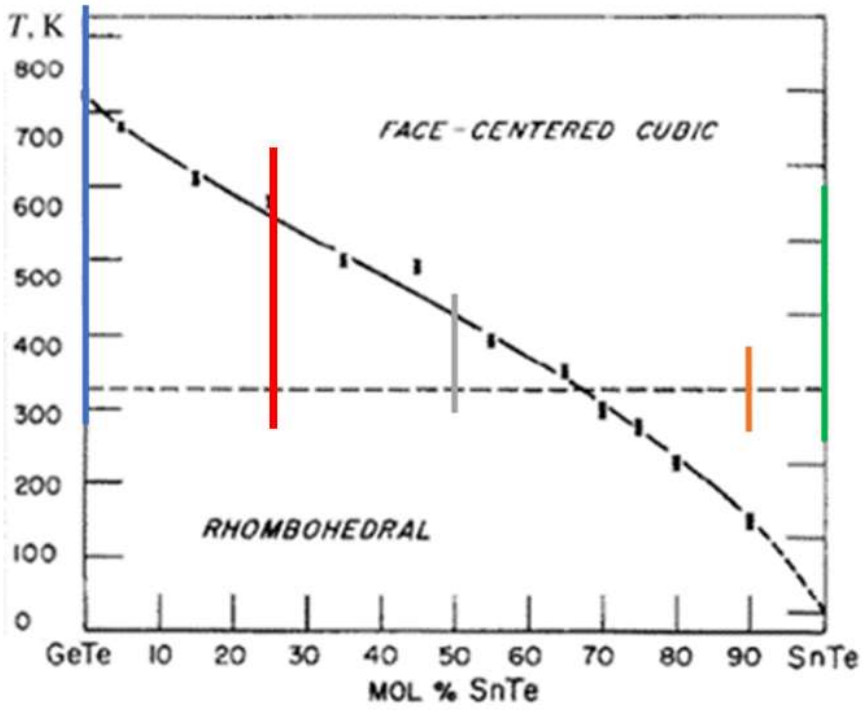

Figure 19. Composition-dependent structure-change diagram of the $Ge_{1-x}Sn_xTe$ system, with GeTe (blue), $Sn_{.25}Ge_{.75}Te$ (red), $Sn_{.5}Ge_{.5}Te$ (grey), $Sn_{.9}Ge_{.1}Te$ (orange), and SnTe (green) marked. Length of lines represent breadth of temperature range for measurements. [36]

Preliminary room-temperature X-ray diffraction analyses were used to establish that each sample had the composition and structure expected: rhombohedral for $Sn_{.25}Ge_{.75}Te$ and $Sn_{.5}Ge_{.5}Te$, and cubic for $Sn_{.9}Ge_{.1}Te$ and SnTe. Two examples of those analyses, depicting XRD patterns for a sample of the cubic structure type and a sample of the rhombohedral structure type, are depicted in **Figures 20** and **21**, which show $Sn_{.5}Ge_{.5}Te$ and SnTe, respectively. The peaks were indexed to either the cubic or rhomborhedral phase, respectively. Comparing the two patterns shows that rhombohedral distortion leads to splitting of the specific peaks that were visible in the cubic structure. Additionally, a secondary phase, which was identified as pure Sn, was also present in scans of SnTe.

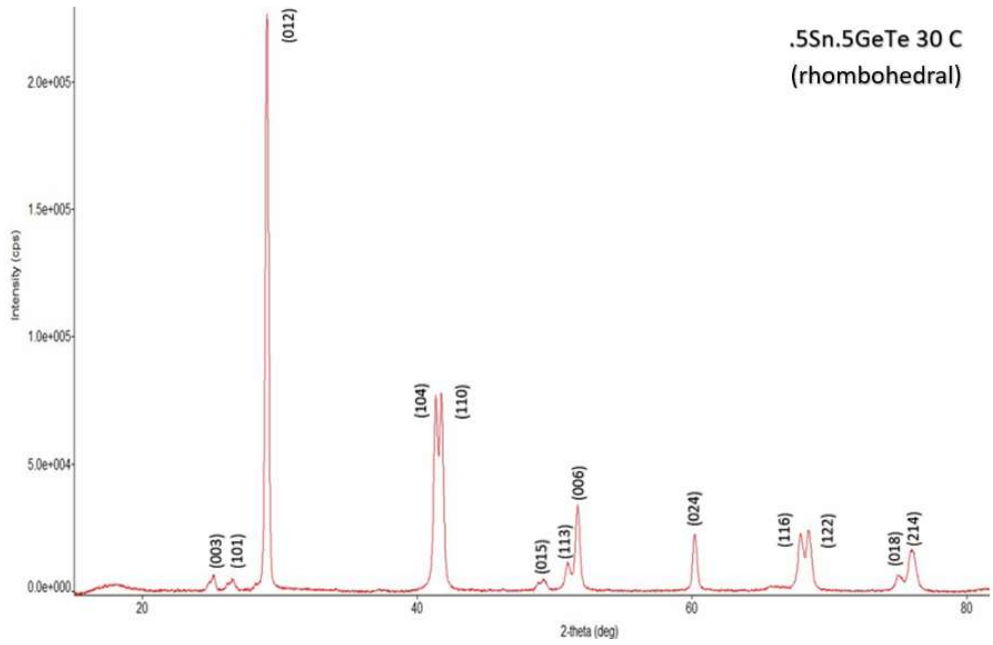

Figure 20. Indexed XRD plot of $Sn_{.5}Ge_{.5}Te$ at 30C, showing the rhombohedral structure type, with its characteristic split peaks.

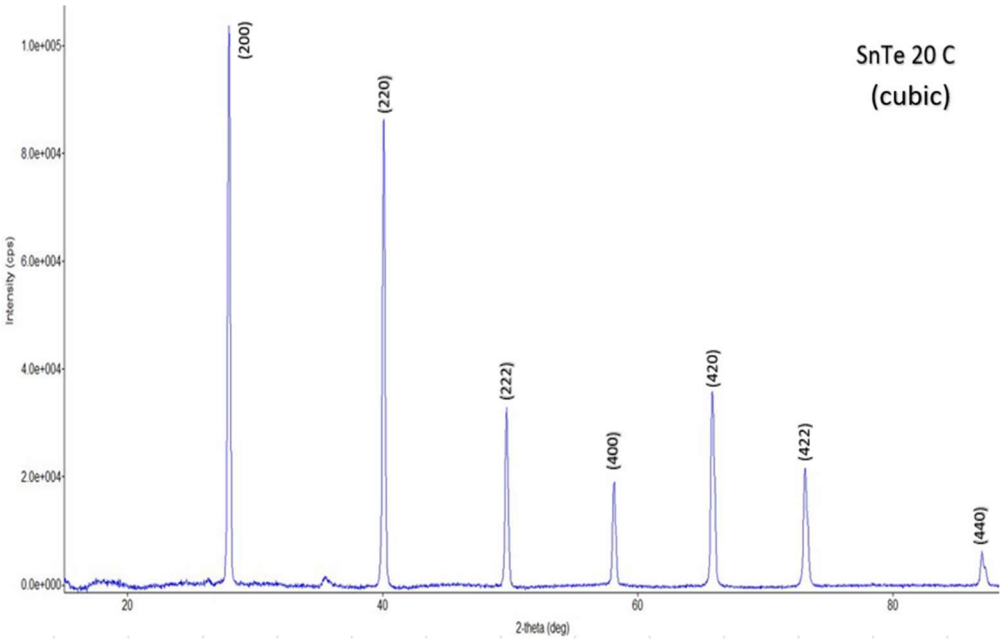

Figure 21. Indexed XRD plot of SnTe at 20C, showing the cubic structure type, with its characteristic single peaks.

The subsequent X-ray diffraction measurements were taken at progressively higher temperatures from 40 to 400 C. These temperature ranges were selected to show rhombohedral to cubic phase change in a sample and to provide a large enough number of data points for analysis of each sample's thermal characteristics. The resulting patterns clearly display peak shifting to lower angles with higher temperatures, as illustrated in **Figure 21**- a pattern caused by the increased length of the lattice parameters at higher temperatures. The X-ray diffraction plot in **Figure 21** also illustrates the phase transition from rhombohedral to cubic in $Sn_{.25}Ge_{.75}Te$ and $Sn_{.5}Ge_{.5}Te$, at temperatures of 220 C and 120 C respectively. Both transitions are indicated by two peaks, (116) and (122), overlapping to an increasing degree until they converge to become one cubic (422) peak.

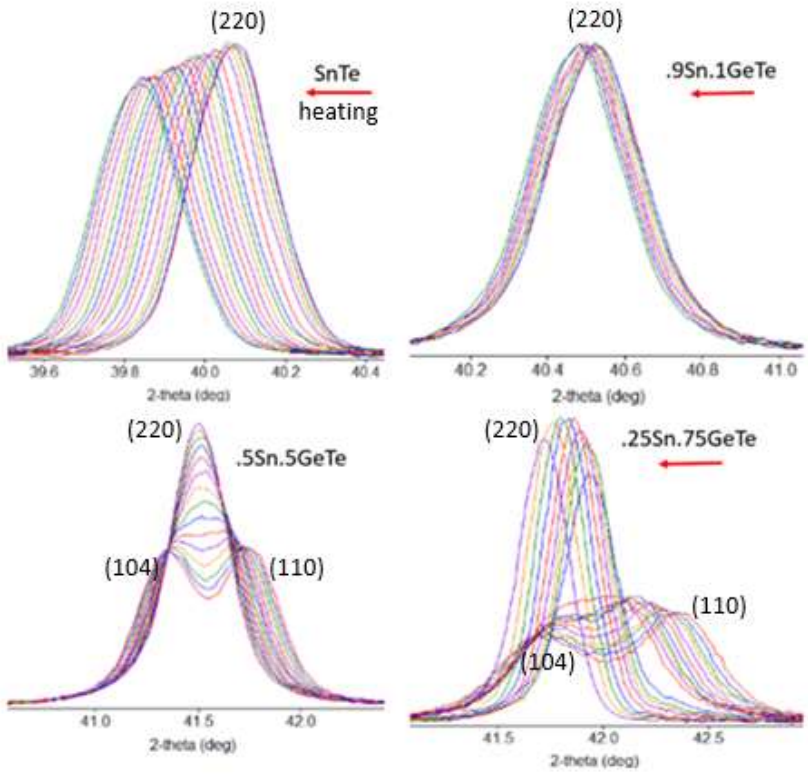

Figure 22. Examples of peak change with temperature for the four analyzed compositions. The red arrows indicate the direction of peak shift with increasing temperature for SnTe and .9Sn.1GeTe samples, while the two peaks merge into one with increasing temperatures in the .5Sn.5GeTe and .25Sn.75GeTe samples, indicating a phase change from the rhombohedral to the cubic structure.

In conjunction with Rigaku PDXL2 X-ray diffraction software, this raw data was used to identify a, b, and c lattice parameters for each sample at each measured temperature. This was a process which required a significant degree of finesse, as PDXL2 often required assistance identifying and indexing peaks, in particular when two or more peaks were overlapping. For consistency and convenience (i.e. the ability to display all parameters on a common plot), the resulting lattice parameters were all converted to hexagonal lattice parameters- a simple matter of multiplying by the square root of 2 or the a and b parameters, or by the square root of 3 for the c parameter- and plotted as a function of temperature in **Figure 23** and **Figure 24**. Based on the lattice parameters,

unit cell volumes for each composition were also plotted as a function of temperature in **Figure 25**.

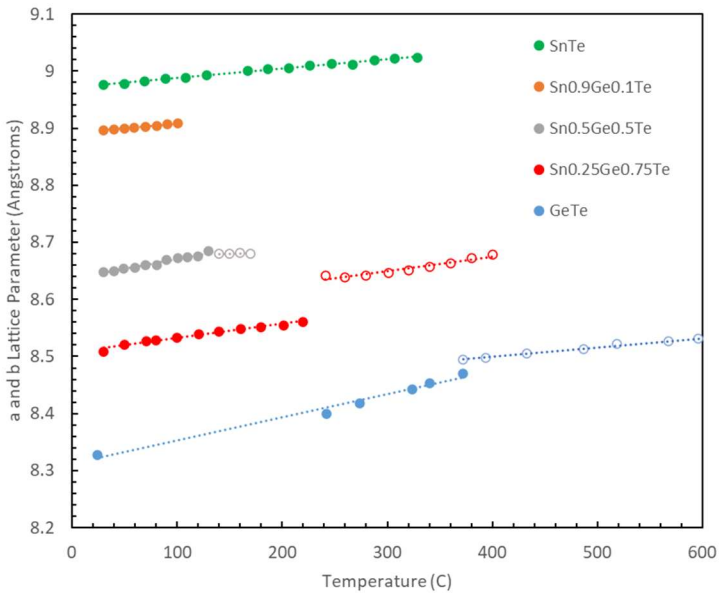

Figure 23. 'a' and 'b' lattice parameters vs. temperature for all measured samples, with GeTe data from literature. Closed circles denote data points recorded before a phase change, open circles denote data points recorded after a phase change. SnTe and Sn0.9Ge0.1Te were Fm3m cubic throughout- the others were R3m rhombohedral at low temperatures and Fm3m cubic after the phase change.

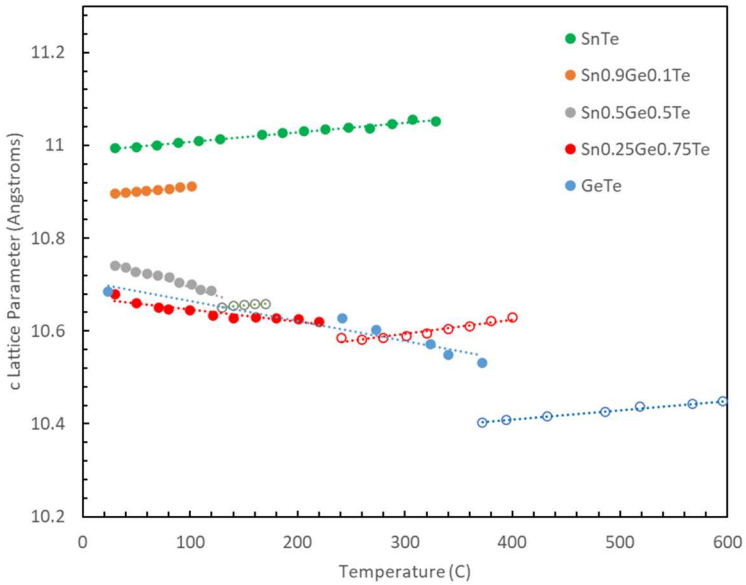

Figure 24. 'c' lattice parameters vs. temperature for all measured samples, with GeTe data from [25]. Closed circles denote data points recorded before a phase change, open circles denote data points recorded after a phase change. SnTe and Sn0.9Ge0.1Te were Fm3m cubic throughout- the others were R3m rhombohedral at low temperatures and Fm3m cubic after the phase change.

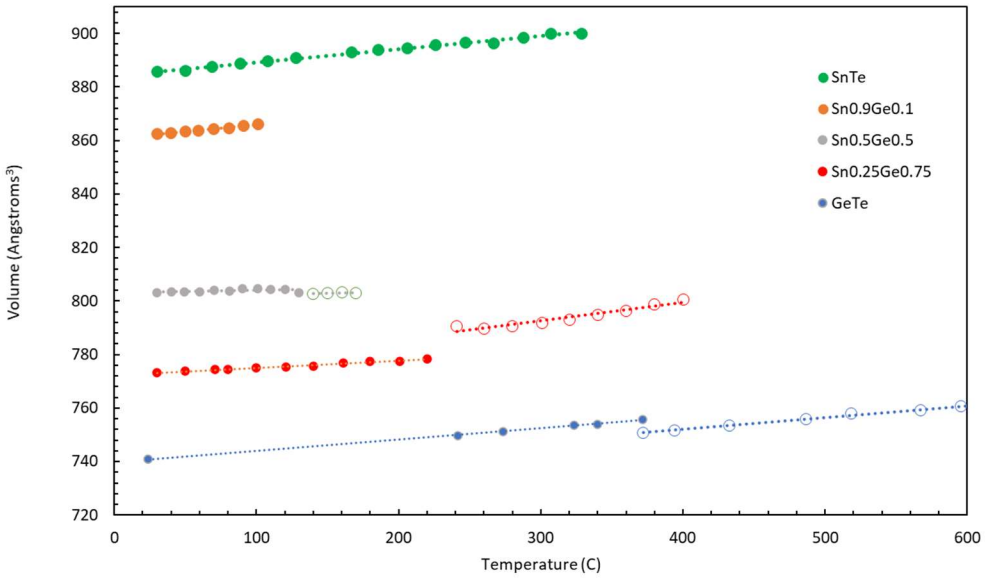

Figure 25. Unit cell volume vs. temperature for all measured samples, with GeTe data from [25]. Closed circles denote data points recorded before a phase change, open circles

Figure 25 (cont'd)
denote data points recorded after a phase change. SnTe and Sn0.9Ge0.1Te were Fm3m cubic throughout- the others were R3m rhombohedral at low temperatures and Fm3m cubic after the phase change.

Several takeaways from these plots are obvious. Immediately apparent is a lattice parameter reduction with increasing Ge content- a fact which accords perfectly with Ge's smaller atomic radius: 211 pm, compared to Sn's 217 pm [50]. Also immediately apparent are phase changes in GeTe, $Sn_{.25}Ge_{.75}Te$, and $Sn_{.5}Ge_{.5}Te$, which appear in the form of discontinuities in the data. The temperature at which each discontinuity occurs is somewhat in line with the literature data shown in **Figure 22, Figure 23** and **Figure 24**. In $Sn_{.25}Ge_{.75}Te$, this is at 240 C, versus approximately 280 C in the literature data, while in $Sn_{.5}Ge_{.5}Te$ this is at around 120 C, versus approximately 160 C in the literature data [36]. The literature-experimental data discrepancy is consistent between samples, perhaps indicating some sort of systematic measurement error.

The way in which lattice parameters change with increasing temperature within each structure type is also consistent with expected behavior. The 'a' parameter increases in a linear way before and after the phase change in samples that exhibit a phase change, which is consistent with the expected steady expansion of the cubic and rhombohedral lattices. In contrast, the 'c' parameter in the rhombohedral samples decreases as the temperature rises towards the phase change point, but increases after the phase change, while it is in the cubic structure. This is also consistent with expected behavior: it indicates that the rhombohedral lattice, which is a distorted cubic lattice, is 'un-distorting' and becoming more cubic as it approaches the phase change. At temperatures above the phase transition, the lattice parameters of samples in the cubic phase are then increasing in the expected linear way after the phase change.

The lattice parameter data allowed for the calculation of the coefficient of thermal expansion (CTE) for each composition through first calculating the volume of the unit cell at each temperature, and then using the resultant data with the equation for the coefficient of thermal expansion

$$\alpha_v = \frac{1}{V}\left(\frac{dV}{dT}\right)$$

in which α_v is the coefficient of thermal expansion, V is the volume of the hexagonal unit cell, and $\frac{dV}{dT}$ is the change in unit cell volume with temperature. The results of these calculations are shown in **Table 2**.

Table 2. Volume Coefficients of Thermal Expansion, in /C

Composition	**Rhombohedral Volumetric CTE C^{-1}**	**Cubic Volumetric CTE C^{-1}**
SnTe	-	5.57E-05
$Sn_{.9}Ge_{.1}Te$	-	5.68E-05
$Sn_{.5}Ge_{.5}Te$	1.15E-05	1.73E-05
$Sn_{.25}Ge_{.75}Te$	3.36E-05	8.89E-05
GeTe	5.67E-05	5.86E-05

The data within Table 2 differs in intriguing ways from the published volume coefficients of thermal expansion for the end-member compounds, GeTe and SnTe, which are in line with reported results for other rock-salt chalcogenides like PbS, PbSe, and PbTe [51].

While $Sn_{.9}Ge_{.1}Te$'s volume CTE differs only slightly from SnTe's, as well as from GeTe's in both rhombohedral and cubic forms, both cubic and rhombohedral $Sn_{.5}Ge_{.5}Te$ have volume CTEs significantly lower than GeTe's. $Sn_{.25}Ge_{.75}Te$ is even more different, with a volume CTE significantly lower than either end member in its rhombohedral form and a volume CTE significantly higher than any other recorded value in its cubic form. There are some interesting

implications for the way the material Grüneisen parameter changes with composition and temperature that follow from these values. Since the Grüneisen parameter increases with an increasing volume CTE, this data suggests that, starting from SnTe, the Grüneisen parameter will first increase, then decrease to a minimum value as the composition approaches $Sn_{.5}Ge_{.5}Te$, increase again to a high-temperature maximum value near $Sn_{.25}Ge_{.75}Te$, and then decrease to a level similar to that found in SnTe as it approaches GeTe.

5. Determination of High-Pressure Properties of the $Ge_{1-x}Sn_xTe$ System

High-pressure X-ray diffraction experiments were conducted as described in section **2.3** to discern the system's composition-dependent compressibility, as well as identify any high-pressure phase transitions. Due to beam time limitations, only two samples were analyzed: $Sn_{.2}Ge_{.8}Te$ and $Sn_{.8}Ge_{.2}Te$, which allowed for the analysis of the effect of high pressures on samples with rhombohedral and cubic structure types, respectively, at standard pressure, as shown in **Figure 25**.

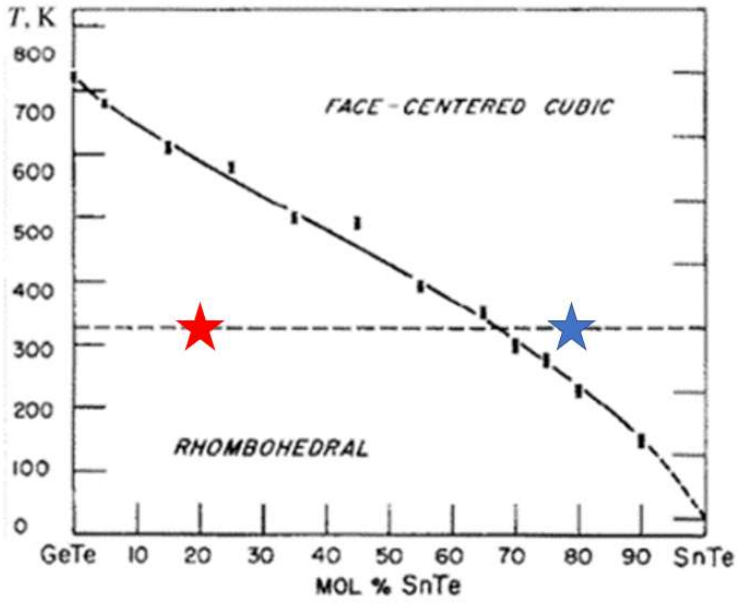

Figure 26. Depiction of the room-temperature composition and structure of both high-pressure samples, adapted from Bierly et. al., with R3m rhombohedral $Sn_{.2}Ge_{.8}Te$ marked in red and Fm3m cubic $Sn_{.8}Ge_{.2}Te$ marked in blue.

The 2D image plate detector on the 13-BM-C beamline at APS collects raw X-ray diffraction data in the form of a 'ring' pattern, as shown below in **Figure 27**, where every ring represents a reflection, or what would be recorded as a peak on a conventional XRD machine with a 1D detector. The detector collects X-ray intensity data using a 2x5 array of 2D image plates, creating

predictable blank areas in the data that were manually 'masked' using Dioptas software prior to commencement of data analysis- the masking visible as red lines and a red circle in **Figure 26**.

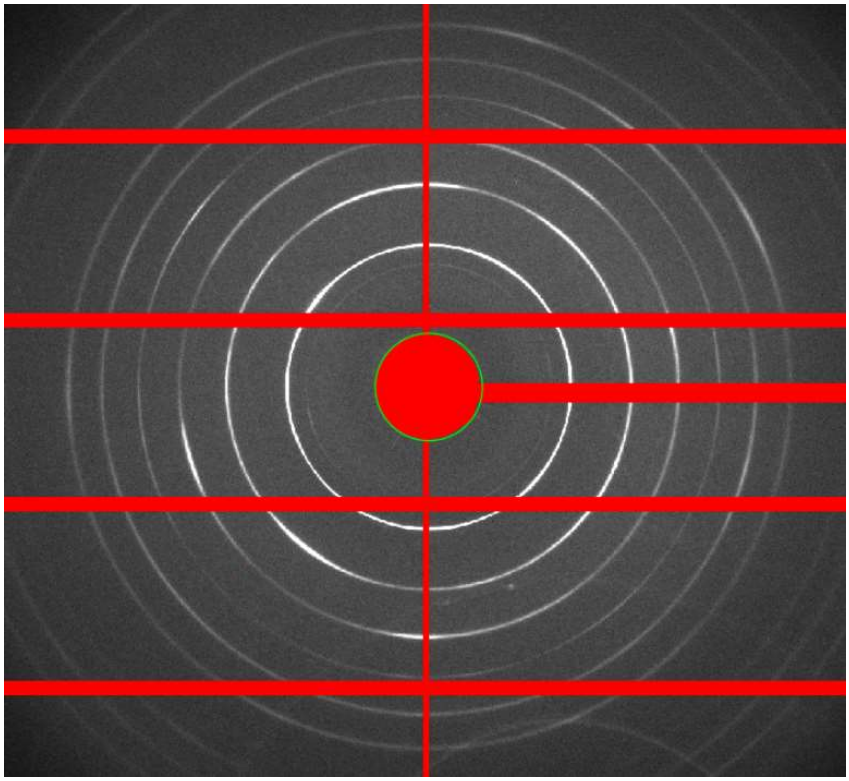

Figure 27. Raw data from 13-BM-C GSECARS beamline for $Sn_{.2}Ge_{.8}Te$ sample. Rings are equivalent to peaks in a conventional X-ray diffraction plot. Red areas indicate detector anomalies that were manually masked for proper analysis.

These 2D patterns were converted to integrated 1D XRD patterns using Dioptas software. Each sample's XRD patterns were laid out in an offset 'waterfall' pattern in order to clearly indicate the way in which each sample changed with pressure, including such events as phase changes and peak shifts. These are shown below in **Figure 28**, which is the waterfall plot for $Sn_{.2}Ge_{.8}Te$, and **Figure 29**, which is the waterfall plot for $Sn_{.8}Ge_{.2}Te$. It is important to note that only the first five reflections could be collected for the $Sn_{.2}Ge_{.8}Te$ sample due to limited diamond anvil cell aperture size, which limited the angles at which data could be gathered.

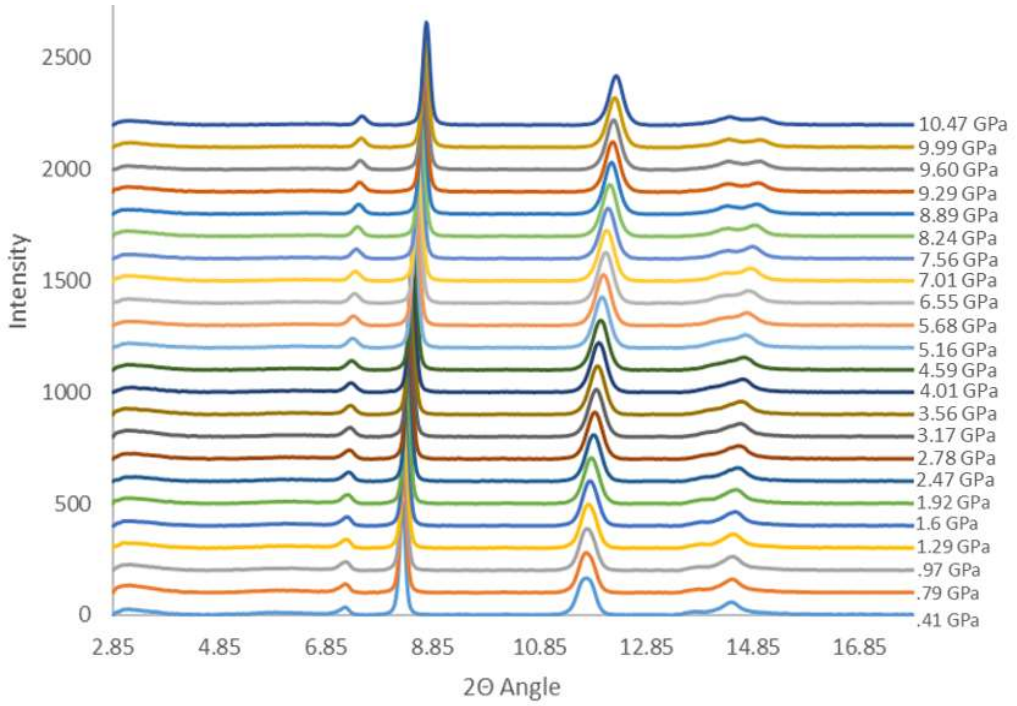

Figure 28. X-ray diffraction plots of $Sn_{.2}Ge_{.8}Te$ between .41 and 10.47 GPa.

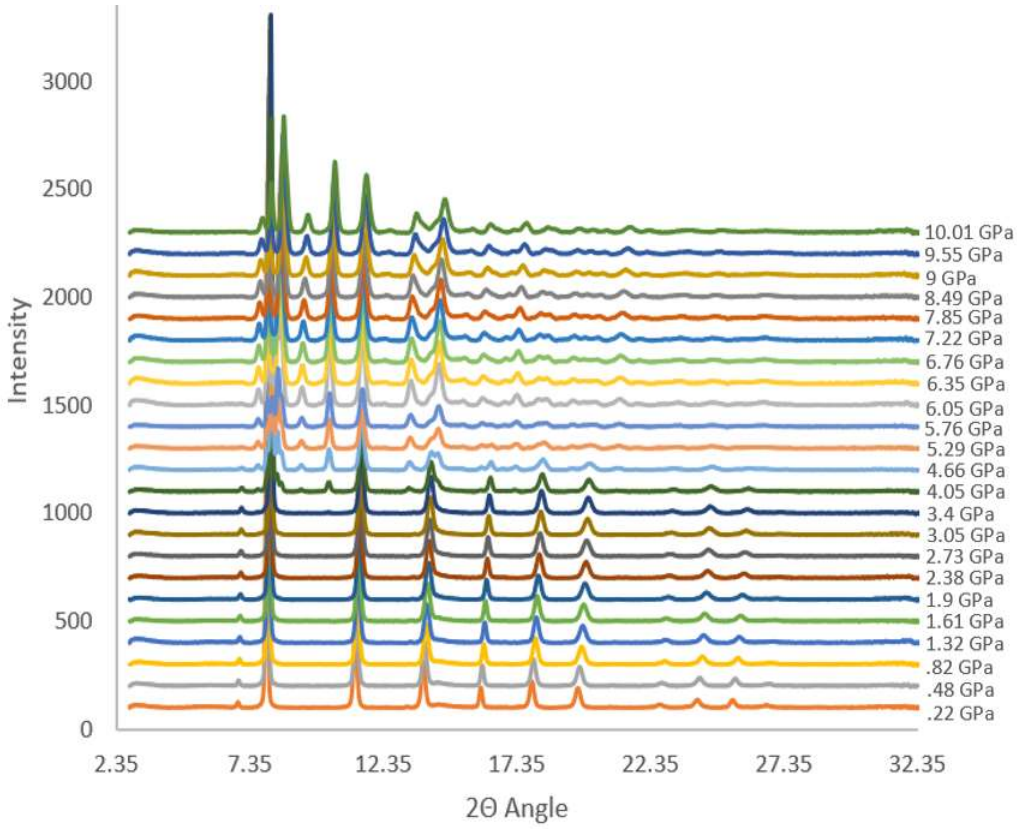

Figure 29. X-ray diffraction plots of $Sn_{.8}Ge_{.2}Te$ between 0.22 and 10.01 GPa.

In **Figure 28**, changes with increasing pressure are as follows: All of the peaks shift to the right with increasing pressure as the unit cell volume is compressed. Although $Sn_{.2}Ge_{.8}Te$ was confirmed to be in the rhombohedral phase before loading in the DAC, the small amount of pressure used during loading of the sample already led to a distortion to a nearly cubic phase. $Sn_{.2}Ge_{.8}Te$'s (006) peak at 14.45 degrees slowly splits as pressure increases, forming increasingly distinct (021) and (202) peaks starting around 4.59 GPa, while the distinct (012) peak at 8.3 degrees shifts farther to the right, eventually reaching 8.74 degrees at 10.47 GPa. A similar peak shift is also apparent in the case of the lower-angle (003) peak, which shifts from 7.18 degrees at .41 GPa to 7.54 degrees at 10.47 GPa. The lower-angle peak shifting is in agreement with the results of high-pressure studies of GeTe, but the peak splitting appears to be a new feature of the $Ge_{1-x}Sn_xTe$ system- it does not appear in published GeTe high-pressure X-ray diffraction studies [52].

Changes with increasing pressure are also revealed in **Figure 29**. Most dramatic of all of these is a transformation from $Sn_{.8}Ge_{.2}Te$'s atmospheric-pressure Fm3m rock-salt cubic phase to a multiphase structure, including both the Fm3m cubic phase and two orthorhombic structures (Cmcm and Pnma), between 3.4 and 4.66 GPa, which is broadly in agreement with published SnTe high-pressure X-ray diffraction studies [53]. As in the case of $Sn_{.2}Ge_{.8}Te$, some peak shifting was apparent, with the (422) peak at 19.6 degrees showing the largest shift, reaching 20.2 degrees at 3.4 GPa as it approached the phase change.

Rietveld refinement functions in Rigaku PDXL2 software were to obtain lattice parameter data for each sample at each pressure- throughout the entire measurement range for $Sn_{.2}Ge_{.8}Te$ using a rhombohedral unit cell, and until the phase change for $Sn_{.8}Ge_{.2}Te$ using a cubic unit cell. The resulting plots, featuring lattice parameters versus pressure for each composition are shown below in **Figure 30, Figure 31, and Figure 32.**

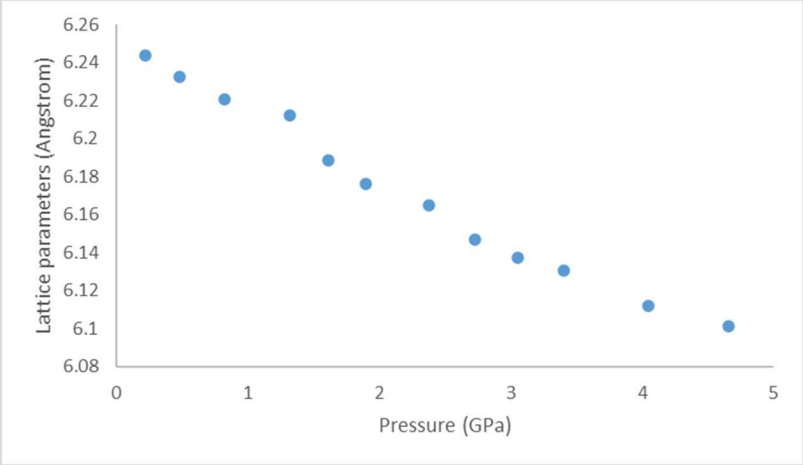

Figure 30. $Sn_{.8}Ge_{.2}Te$ Lattice parameter vs. Pressure plot for a=b= c parameters.

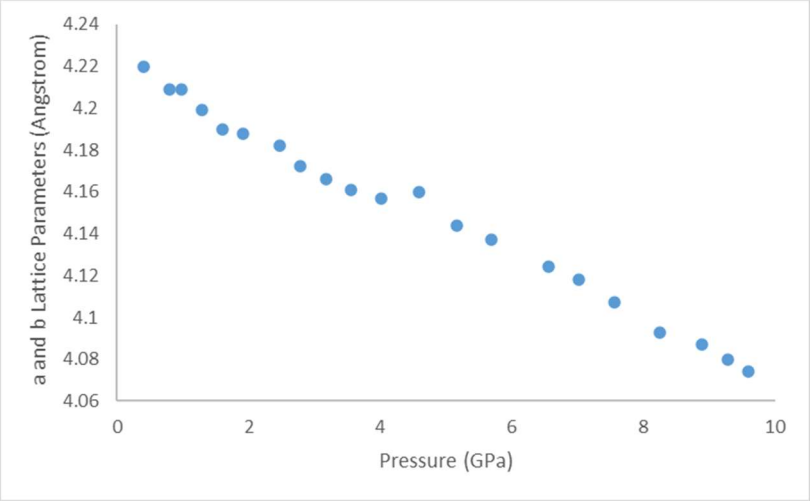

Figure 31. $Sn_{.2}Ge_{.8}Te$ Lattice parameter vs. Pressure plot for a = b parameters.

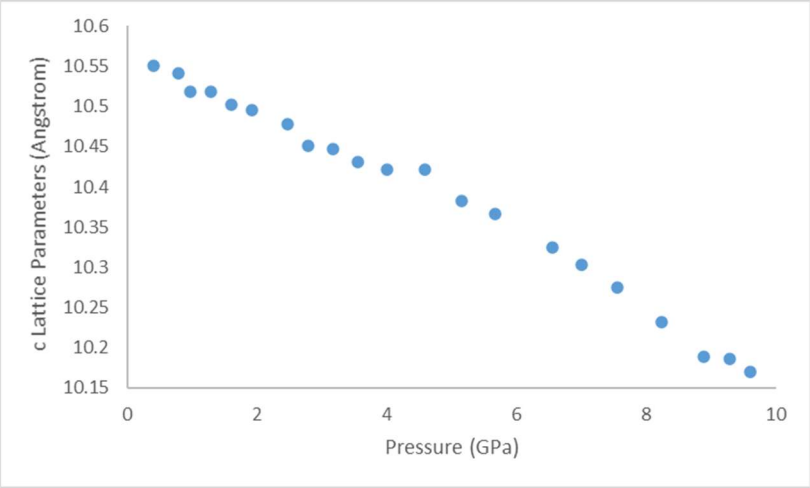

Figure 32. $Sn_{.2}Ge_{.8}Te$ Lattice parameter vs. Pressure plot for c parameter only.

All three plots show a trend towards smaller lattice parameters with increasing pressure- a trend entirely consistent with the relation between pressure on a solid and its volume, as well as published data from SnTe and GeTe high-pressure X-ray diffraction studies [52, 53].

This data was also used with the 2nd-order Birch-Murnagham equation to calculate the bulk modulus of each sample. This was accomplished by use of a program called EoSFit7, which was developed to find equations of state for minerals. EoSFit7 functions by fitting an estimated equation-of-state curve to provided experimental unit cell volume and pressure data, providing a value for the bulk modulus of each fitted sample. The fitted curves generated by the software are shown below in **Figure 33** and **Figure 34**.

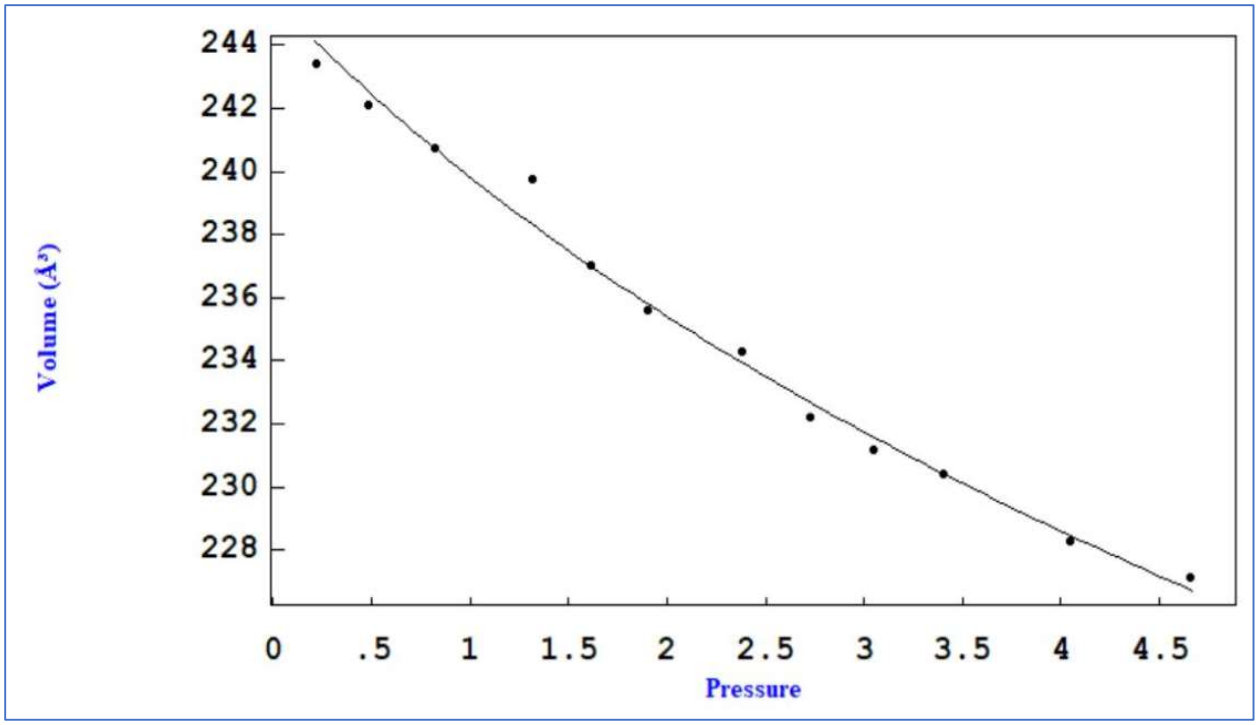

Figure 33. Fitted equation-of-state curve for $Sn_{.2}Ge_{.8}Te$ sample generated with EoSFit7 software.

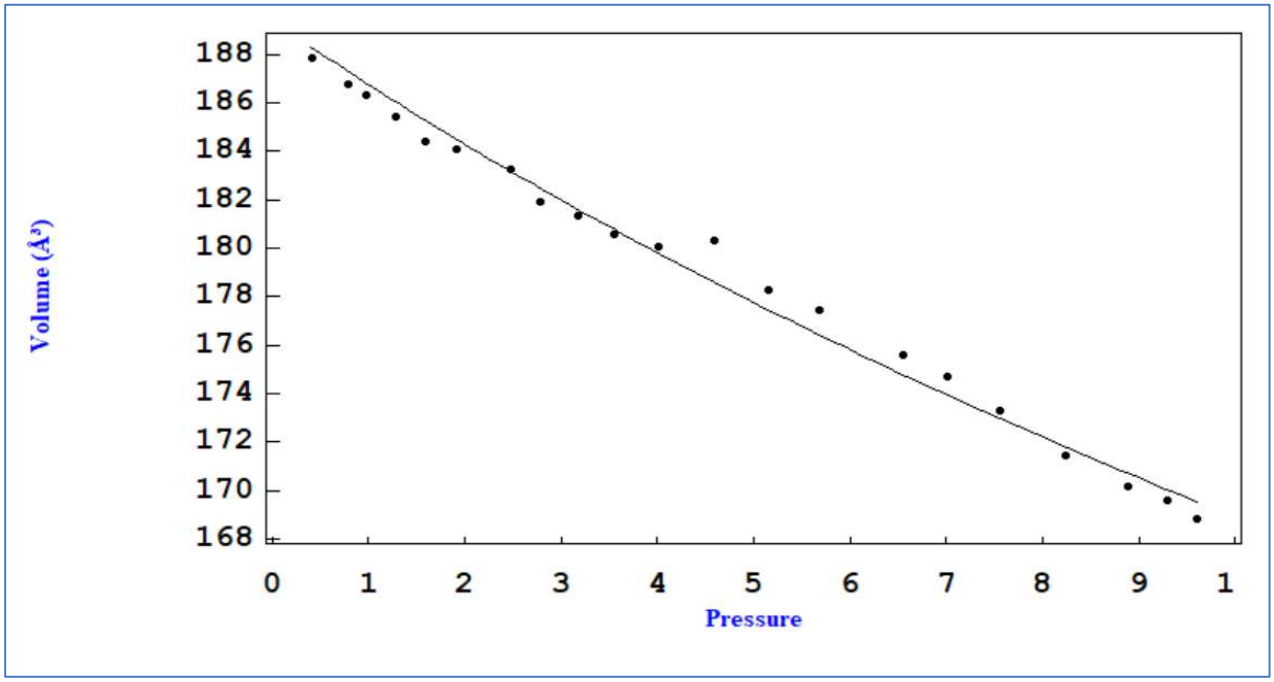

Figure 34. Fitted equation-of-state curve for $Sn_{.8}Ge_{.2}Te$ sample generated with EoSFit7 software. A discontinuity is visible at around 4.5 Gpa- this is likely due to lattice parameter fitting errors, which would produce an incorrect volume value.

The fitted 2nd-order Birch-Maugham data for both samples is displayed below, in **Table 3**.

Table 3. Birch-Maugham data for both high-pressure X-ray diffraction samples.

Composition	**V_0 (A^3)**	**K' (GPa)**
$Sn_{.8}Ge_{.2}Te$	245.5	36.89
$Sn_{.2}Ge_{.8}Te$	189.38	69.49

V_0, or original pressure unit cell volume data, is consistent with other analyses, with the larger atomic radius of Sn again inducing greater unit cell sizes with an increase in alloy Ge content. The change in K', or bulk modulus, with Sn and Ge content changes are broadly consistent with values previously established during the RUS measurement series described above- likely due to the structural properties of the rhombohedral and cubic structures themselves, as also described in Chapter 3.

6. Results of Bridgman Single-Crystal Synthesis

Essential to the objective of ascertaining phonon behavior and its connections to thermal and transport properties is the experimental technique of inelastic neutron scattering (INS). Simply put, INS utilizes the diffraction of neutrons of a known wavevector emitted from a neutron source to characterize the phonon behavior of a given material [54]. This process depends on the tendency of neutrons to scatter inelastically when interacting with a crystalline solid's phonons, meaning that the neutron will either gain or lose energy upon scattering [54]. This energy change in turn modifies the wavevectors of the scattered neutrons- information which can in turn be used to determine the frequencies of the phonons in question [54].

To properly utilize INS, however, sizable sample dimensions are critical. This is essentially because neutrons scatter from atomic nuclei alone, rather than both the electron shells and nuclei, as X-rays do [54]. Since atomic nuclei are a miniscule fraction of overall atomic volume, neutron-nucleus contact and subsequent scattering is a very unlikely event. Therefore, to produce a reasonably large quantity of scattered neutrons, one must place a very large quantity of atoms in front of the incident neutron beam. This necessitates a bulk sample.

INS was to be used for the investigation of the $Ge_{1-x}Sn_xTe$ system. $Ge_{1-x}Sn_xTe$ was selected due to the presence of a room temperature cubic-to-rombohedral transition in the vicinity of $Ge_{.3}Sn_{.7}Te$, which would provide interesting information on the phonon dynamics of structural changes in III-V semiconductors. It was accordingly necessary to create bulk single crystal $Ge_{1-x}Sn_xTe$ ingots- bulk to provide the necessary quantity of atoms for reliable neutron interaction, as

described above, and single crystal to eliminate sources of phonon scattering such as grain boundaries. As in previous investigations, this was accomplished via the Bridgman method.

There were 25 attempts to grow bulk single crystals of various compositions within the $Ge_{1-x}Sn_xTe$ system using the Bridgman system for INS measurements to be performed at Duke University. A full list of successfully completed (though not necessarily single-crystal) Bridgman samples is shown below, in **Table 4**, along with several of their most important growth variables.

Table 4. All attempts at single-crystal growth via Bridgman furnace, showing their most important growth variables, results of growth, and notes on selected samples.

Growth Attempt	Composition	Mass (g)	Tube Diameter (mm)	Soak Temperature (C)	Translation Rate (mm/s)	Result	Notes
1	$Sn_{.8}Ge_{.2}Te$	10.08	10	850	0.001	Polycrystal	
2	$Sn_{.8}Ge_{.2}Te$	10.00	10	850	0.001	Polycrystal	
3	$Sn_{.8}Ge_{.2}Te$	10.00	10	850	0.001	-	Lost
4	$Sn_{.8}Ge_{.2}Te$	9.96	10	850	0.001	Polycrystal	
5	$Sn_{.8}Ge_{.2}Te$	9.98	10	850	0.001	Polycrystal	
6	$Sn_{.8}Ge_{.2}Te$	9.99	12.7	850	0.001	-	Lost
7	$Sn_{.8}Ge_{.2}Te$	10.01	12.7	850	0.001	Polycrystal	
8	$Sn_{.8}Ge_{.2}Te$	9.98	12.7	850	0.001	Polycrystal	
9	$Sn_{.8}Ge_{.2}Te$	10.00	10	850	0.001	Polycrystal	
10	$Sn_{.7}Ge_{.3}Te$	9.96	10	900	0.001	Polycrystal	
11	$Sn_{.9}Ge_{.1}Te$	9.99	10	900	0.001	-	Lost
12	$Sn_{.7}Ge_{.3}Te$	10.03	10	1000	0.001	Large-grained polycrystal	
13	$Sn_{.9}Ge_{.1}Te$	9.98	10	1000	0.001	Large-grained polycrystal	
14	$Sn_{.8}Ge_{.2}Te$	10.01	10	1000	0.001	Large-grained polycrystal	
15	$Sn_{.7}Ge_{.3}Te$	9.28	10	1000	0.0001	Large-grained polycrystal	Sent to Duke
16	$Sn_{.6}Ge_{.4}Te$	20.00	10	1000	0.0001	Single crystal	
17	$Sn_{.8}Ge_{.2}Te$	20.00	10	1000	0.0001	Single crystal	
18	$Sn_{.8}Ge_{.2}Te$	20.17	10	1000	0.0001	Single crystal	Sent to Duke
19	$Sn_{.6}Ge_{.4}Te$	20.00	10	1000	0.0001	Single crystal	Sent to Duke
20	$Sn_{.8}Ge_{.2}Te$	10.00	10	1000	0.01	Polycrystal	
21	$Sn_{.8}Ge_{.2}Te$	19.99	10	1000	0.0001	-	Lost
22	$Sn_{.8}Ge_{.2}Te$	19.97	10	1000	0.0001	Single crystal	Sent to Duke
23	$Sn_{.8}Ge_{.2}Te$	10.01	10	1000	0.0001	Single crystal	

As previously mentioned, the conditions for the first nine crystal growth attempts were set using a trial-and-error method. The furnace was raised to 850 C, above the melting temperature of the

selected $Ge_{1-x}Sn_xTe$ compounds, the crucible was lowered through the furnace at the slowest continuous rate described above (.001 mm/s), and the resulting ingots were analyzed as described above. Each of these growth attempts resulted in a polycrystalline sample, as depicted below in **Figure 34**, which shows an image of sample number 20, an attempt to test the ability to quickly produce a bulk single crystal. Easily seen is the texture of the fracture surface produced when a piece of the sample broke off the main ingot during extraction from the crucible. The 'wood-grain quality of this fracture surface is visual evidence of a microstructure comprised of ~.1 mm-diameter grains. XRD studies of powdered fragments taken from different areas of the polycrystalline samples confirmed that the composition was homogenous throughout, validating the convection mixing plan.

Figure 35. Image of a fracture surface of sample 20, a polycrystalline $Sn_{.8}Ge_{.2}Te$ ingot, showing a 'wood-grain' texture that stems from a structure comprised of a multitude of small grains.

All subsequent attempts (17), were conducted after the discovery of a paper containing a temperature gradient value that produced a successful growth- 32 degrees Celsius per centimeter [42]. An extensive growth program followed in an attempt to leverage this information into a set of completed single crystals. An example of an intermediate result, generated using this temperature gradient value, is sample 13, shown below in **Figure 35**, which showed large, shiny faceted surfaces where it fractured during sectioning- a characteristic sign of at least a large single grain, if not a whole single crystal ingot. EDS measurements conducted on one half of the sectioned and fractured sample confirmed an acceptable degree of homogeneity, but a fracture that occurred while removing the sample from the EDS stage displayed a 'woody' multi-grained microstructure similar to the one described in the preceding section. More changes in furnace and motion settings were therefore required to create a sample with the required properties.

Figure 36. Image of a fracture surface of sample 13, a large-grained polycrystalline $Sn_{.9}Ge_{.1}Te$ ingot, showing fracture along the boundaries of both large and small grains within the ingot- the large grains denoted by faceting, the small grains denoted by a 'woody' appearance.

An example of a single-crystal ingot of the type suitable for INS measurements is shown below, in **Figure 36**.Grown using a very sharp temperature gradient of 48 C/cm in the Crystal Systems Corporation SCX-1100 tube furnace, sample 18 displayed a notable lack of visible defects when compared to earlier growth efforts. Upon extraction from the crucible, every visible fracture surface in the sample was faceted, as seen in **Figure 36**, a clear indication of single crystallinity. EDS analysis of a sectioned segment of sample 18, shown below in **Figure 38**, also indicated adequate sample homogeneity. Further proof of single crystallinity was provided via imaging the sample 18 ingot's polished surface using MSU's Laue X-ray backscatter camera, one image of which is also shown below, in **Figure 37**. These analyses confirmed that the entire ingot was one crystal- a conclusion further confirmed by additional Laue analysis with up-to-date equipment at Duke.

Figure 37. Image of a fracture surface in sample 18, a single-crystal $Sn_{.8}Ge_{.2}Te$ ingot, showing extensive faceting and no areas of small-grained, 'woody' texture, indicating that the entire sample is comprised of one large grain.

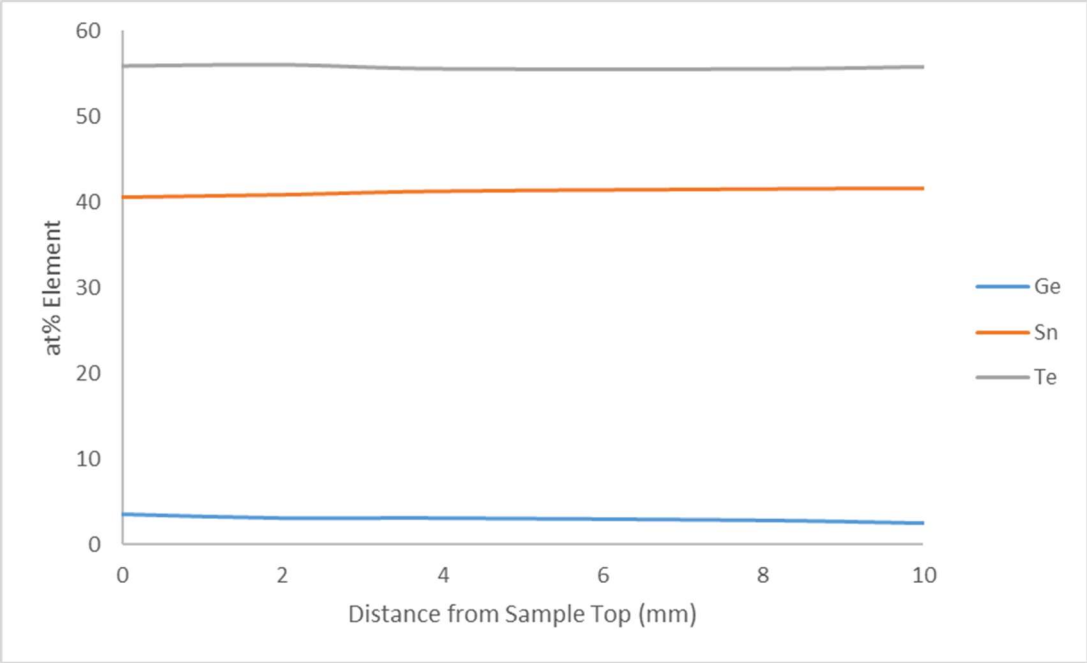

Figure 38. Sample 18 Energy Dispersion Spectroscopy Data, showing little variation in elemental composition over the length of the entire sample.

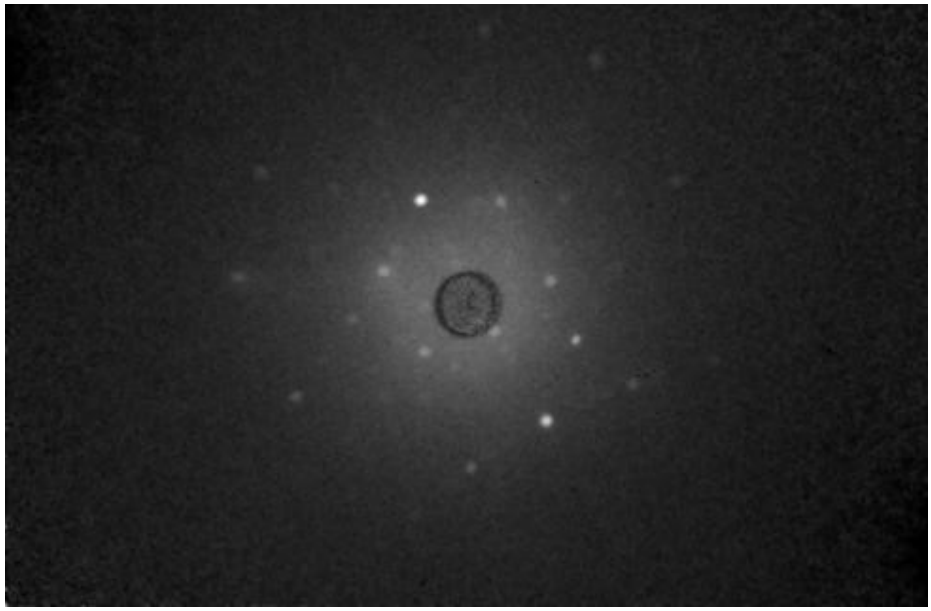

Figure 39. Sample 18 Laue camera image, showing discrete points- a characteristic feature of a single crystal. A polycrystalline sample would instead feature 'rings' around the camera aperture, which is visible as a circle in the middle of the image.

7. Conclusion

Resonant ultrasound spectroscopy measurements on polycrystalline samples in the $Ge_{1-x}Sn_xTe$ series allowed for the elucidation of the ways in which several important constants change with the composition and atomic structure of the alloy. Specifically, quantities like C11 and C44, Young's modulus, the bulk modulus, and speed of sound within the material all behave in the same way: they decrease with increasing Sn content in the rhombohedral phase, but radically increase after enough Sn is added to cause a transition to the cubic phase. This suggests that the rhombohedral structure is inherently softer than the cubic structure- but within each structure, composition dominates. However, testing of additional compositions – in particular of a Ge-rich sample in the cubic phase - is required to confirm these suppositions.

The lattice parameters of $Ge_{1-x}Sn_xTe$ samples were obtained from high-temperature X-ray diffraction, allowing for the identification of changes in the coefficient of thermal expansion at different compositions. In the rhombohedral phase, we observed an increase in the coefficient of thermal expansion with decreasing Sn percentage. However, in the cubic phase, there was a peculiar and radical increase coefficient of thermal expansion from SnTe towards the intermediate compositions, such as $Ge_{.5}Sn_{.5}Te$, before a rapid decrease to a level relatively similar to SnTe's, as the composition approached GeTe. Further work must be done to understand the underlying cause of this unusual trend.

Finally, high-pressure X-ray diffraction analyses allowed for the characterization, via the 2nd order Burch-Murnagham equation, of the bulk moduli of two different compositions, representing both rhombohedral and cubic structures at room temperature and pressures-

$Sn_{.2}Ge_{.8}Te$ (rhombohedral) and $Sn_{.8}Ge_{.2}Te$ (cubic). This allowed the high-pressure X-ray data to serve as a further check of the accuracy of elastic constants calculated using resonant ultrasound spectroscopy. The bulk modulus of the $Sn_{.25}Ge_{.75}Te$ sample successfully analyzed using resonant ultrasound spectroscopy is a reasonable match for the $Sn_{.2}Ge_{.8}Te$ rhombohedral sample analyzed by means of high-pressure X-ray diffraction- 34.0 GPa vs. 36.89 GPa- but the bulk modulus value of the $Sn_{.8}Ge_{.2}Te$ sample, 69.49, does not comport with expectations from RUS measurements. Significant work is required to eliminate this disagreement.

Additionally, an extensive test program allowed for the reliable creation of bulk single crystal ingots of compositions of interest- namely, those around the room-temperature phase change composition, $Sn_{.7}Ge_{.3}Te$. These single crystals are currently being used for inelastic neutron scattering measurements at Oak Ridge National Laboratory, which will in turn allow for greater understanding of the $Ge_{1-x}Sn_xTe$ system's phonon characteristics.

All of this information has expanded the knowledge of material properties required to understand the trends in lattice thermal conductivity within the $Ge_{1-x}Sn_xTe$ system, and, along with it, the list of methods by which lattice thermal conductivity may be modified and controlled: a key objective of many studies into thermoelectric material candidates, and an important step required for the broader real-world implementation of thermoelectrical technologies.

BIBLIOGRAPHY

BIBLIOGRAPHY

1. Beretta, D., et al., *Thermoelectrics: From history, a window to the future.* Materials Science and Engineering: R: Reports, 2019. **138**.

2. Zhao, D. and G. Tan, *A review of thermoelectric cooling: Materials, modeling and applications.* Applied Thermal Engineering, 2014. **66**(1-2): p. 15-24.

3. Zhang, X. and L.-D. Zhao, *Thermoelectric materials: Energy conversion between heat and electricity.* Journal of Materiomics, 2015. **1**(2): p. 92-105.

4. Alfred, *Thermoelectric Generator Charge Carriers*, thermoelectric-generator-charge-carriers-768x675, Editor. 2019, Applied Thermoelectric Solutions Michigan. p. Visual diagram of thermoelectrical generator function.

5. DiSalvo, F.J., *Thermoelectric cooling and power generation.* Science, 1999. **285**(5428): p. 703-6.

6. Lange, R.G. and W.P. Carroll, *Review of recent advances of radioisotope power systems.* Energy Conversion and Management, 2008. **49**(3): p. 393-401.

7. NASA/JPL, *Diagram: Radioisotope Thermoelectric Generator*, 800px-Voyager_Program_-_RTG_diagram_2, Editor. 1978, NASA: Voyager Bulletin, no. 13.

8. Johnson, T. and A. Joshi, *Review of Vehicle Engine Efficiency and Emissions.* SAE International Journal of Engines, 2018. **11**(6): p. 1307-1330.

9. Alessandro Franco, A.R., *Combined cycle plant efficiency increase based on the optimization of the heat recovery steam generator operating parameters.* International Journal of Thermal Sciences, 2001. **41**.

10. Gaultois, M.W., et al., *Data-Driven Review of Thermoelectric Materials: Performance and Resource Considerations.* Chemistry of Materials, 2013. **25**(15): p. 2911-2920.

11. Heremans, J.P., et al., *Enhancement of thermoelectric efficiency in PbTe by distortion of the electronic density of states.* Science, 2008. **321**(5888): p. 554-557.

12. Li, J.-F., et al., *High-performance nanostructured thermoelectric materials.* NPG Asia Materials, 2010. **2**(4): p. 152-158.

13. Biswas, K., et al., *High-performance bulk thermoelectrics with all-scale hierarchical architectures.* Nature, 2012. **489**(7416): p. 414-8.

14. Toberer, E.S., A. Zevalkink, and G.J. Snyder, *Phonon engineering through crystal chemistry.* Journal of Materials Chemistry, 2011. **21**(40).

15. R. G. Schwartz, H.S., B. C. Gerstein *Thermal Study of II-IV Semiconductors : Heat Capacity and Thermodynamic Functions of Mg2Pb from 5-300K.* JOURNAL OF SOLID STATE CHEMISTRY, 1971. **3**: p. 533-540.

16. Balakirev, F.F., et al., *Resonant ultrasound spectroscopy: The essential toolbox.* Rev Sci Instrum, 2019. **90**(12): p. 121401.

17. Minnich, A.J., et al., *Thermal conductivity spectroscopy technique to measure phonon mean free paths.* Phys Rev Lett, 2011. **107**(9): p. 095901.

18. Eesley, G.L., et al., *Relaxation time of the order parameter in a high-temperature superconductor.* Phys Rev Lett, 1990. **65**(27): p. 3445-3448.

19. Klemens, P.G., *Heat-Conduction in Solids by Phonons.* Thermochimica Acta, 1993. **218**(218): p. 247-255.

20. Stacey, F.D. and J.H. Hodgkinson, *Thermodynamics with the Grüneisen parameter: Fundamentals and applications to high pressure physics and geophysics.* Physics of the Earth and Planetary Interiors, 2019. **286**: p. 42-68.

21. Jacobsson, T.J., et al., *Determination of Thermal Expansion Coefficients and Locating the Temperature-Induced Phase Transition in Methylammonium Lead Perovskites Using X-ray Diffraction.* Inorg Chem, 2015. **54**(22): p. 10678-85.

22. West, A.R., *Solid State Chemistry and its Applications, Second Edition* 2014, West Sussex, United Kingdom: John Wiley & Sons, Ltd.

23. Perumal, S., S. Roychowdhury, and K. Biswas, *High performance thermoelectric materials and devices based on GeTe.* Journal of Materials Chemistry C, 2016. **4**(32): p. 7520-7536.

24. Oganov, A.R. and C.W. Glass, *Crystal structure prediction using ab initio evolutionary techniques: principles and applications.* J Chem Phys, 2006. **124**(24): p. 244704.

25. Johnson, R.A., W.T. Morgan, and S.R. Rocklin, *Design Ground Test and Flight Test of Snap 10a First Reactor in Space.* Nuclear Engineering and Design, 1967. **5**(1): p. 7-&.

26. Li, G., et al., *Micro- and Macromechanical Properties of Thermoelectric Lead Chalcogenides.* ACS Applied Materials & Interfaces, 2017. **9**(46): p. 40488-40496.

27. Gidlow, D.A., *Lead toxicity.* Occup Med (Lond), 2004. **54**(2): p. 76-81.

28. Vedeneev, V.P., S.P. Krivoruchko, and E.P. Sabo, *Tin telluride based thermoelectrical alloys.* Semiconductors, 1998. **32**(3): p. 241-244.

29. System, T.S.T.-T., *R.C. Sharma, Y.A. Chang.* Bulletin of Alloy Phase Diagrams, 1986. **7**.

30. Xing, G., et al., *Thermoelectric properties of p-type cubic and rhombohedral GeTe.* Journal of Applied Physics, 2018. **123**(19).

31. Taylor, A., *Biochemistry of tellurium.* Biol Trace Elem Res, 1996. **55**(3): p. 231-9.

32. Kretsinger, R.H., V.N. Uversky, and E.A. Permyakov, *Encyclopedia of Metalloproteins*. 2013.

33. Suwardi, A., et al., *Tailoring the phase transition temperature to achieve high-performance cubic GeTe-based thermoelectrics.* Journal of Materials Chemistry A, 2020. **8**(36): p. 18880-18890.

34. Liu, Z., et al., *Phase-transition temperature suppression to achieve cubic GeTe and high thermoelectric performance by Bi and Mn codoping.* Proc Natl Acad Sci U S A, 2018. **115**(21): p. 5332-5337.

35. Volykhov, A.A., L.V. Yashina, and V.I. Shtanov, *Phase relations in pseudobinary systems of germanium, tin, and lead chalcogenides.* Inorganic Materials, 2006. **42**(6): p. 596-604.

36. J. N. Bierly, L.M., O. Beckman, *The continuous rhombohedral-cubic transformation in GeTe-SnTe alloys.* Acta Metallurgica, 1963. **11**.

37. W. Rehwald, G.K.L., *Ultrasonic studies of phase transitions in the tin telluride-germanium telluride system SnxGe1-xTe.* Journal of Physics C: Solid State Physics, 1975. **8**.

38. Wu, C.C., N.J. Ferng, and H.J. Gau, *Thermoelectric properties of Ge1−xSnxTe crystals grown by vertical Bridgman method.* Journal of Crystal Growth, 2007. **304**(1): p. 127-132.

39. Guillon, O., et al., *Field-Assisted Sintering Technology/Spark Plasma Sintering: Mechanisms, Materials, and Technology Developments.* Advanced Engineering Materials, 2014. **16**(7): p. 830-849.

40. Zevalkink, A., et al., *A practical field guide to thermoelectrics: Fundamentals, synthesis, and characterization.* Applied Physics Reviews, 2018. **5**(2).

41. Zadler, B.J., et al., *Resonant Ultrasound Spectroscopy: theory and application.* Geophysical Journal International, 2004. **156**(1): p. 154-169.

42. Schwarz, R.B. and J.F. Vuorinen, *Resonant ultrasound spectroscopy: applications, current status and limitations.* Journal of Alloys and Compounds, 2000. **310**: p. 243-250.

43. Peng, W., Balodhi, Ashiwini, Zevalkink, Alexandra, *High-temperature elastic moduli: a tool for understanding chemical bonding in thermoelectric materials.* Chemical Communications (in preparation), 2020.

44. Peter Capper, P.R., ed. *Crystal Growth Technology: Semiconductors and Dielectrics*. 2010, Wiley-VCH GmbH Weinheim.

45. Stockbarger, D.C., *The production of large single crystals of lithium fluoride.* Review of Scientific Instruments, 1936. **7**(3): p. 133-136.

46. Cepheiden, *Bridgman-Stockbarger Technique*, Bridgman-Stockbarger-Verfahren.svg, Editor. 2018: Wikipedia.

47. Peng, W., et al., *Lattice hardening due to vacancy diffusion in (GeTe)mSb2Te3 alloys.* Journal of Applied Physics, 2019. **126**(5).

48. Schmidt, R.D., et al., *High-temperature elastic moduli of thermoelectric SnTe1±x – y SiC nanoparticulate composites.* Journal of Materials Science, 2013. **48**(23): p. 8244-8258.

49. H. WIEDEMEIER, P.A.S., *The Thermal Expansion of GeS and GeTe.* Z. anorg. allg. Chem, 1977. **431**: p. 299-304.

50. Information, N.L.o.M.N.C.f.B. *Periodic Table of Elements*. 2021; Available from: https://pubchem.ncbi.nlm.nih.gov/periodic-table/.

51. Skelton, J.M., et al., *Thermal physics of the lead chalcogenides PbS, PbSe, and PbTe from first principles.* Physical Review B, 2014. **89**(20).

52. Kagdada, H.L., et al., *Structural stability, dynamical stability, thermoelectric properties, and elastic properties of GeTe at high pressure.* Physical Review B, 2018. **97**(13).

53. Ivanova, A.G., et al., *Structural phase transitions and the equation of state of SnTe at high pressures up to 2 mbar.* JETP Letters, 2019. **106**(10): p. 662-666.

54. Hudson, B.S., *Vibrational spectroscopy using inelastic neutron scattering: Overview and outlook.* Vibrational Spectroscopy, 2006. **42**(1): p. 25-32.